

APPLICATION OF LOCAL TRANSMISSION LINE MODELLED
METASURFACES AND COMPARISON TO HUYGENS-FRESNEL PRINCIPLE
MODELLED METASURFACES

by

Matthew J. Trusnovic

A thesis submitted to the faculty of
The University of North Carolina at Charlotte
in partial fulfillment of the requirements
for the degree of Master of Science in
Electrical Engineering

Charlotte

2021

Approved by:

Dr. Kathryn Weldon

Dr. Mario Mencagli

Dr. Ed Stokes

©2021
Matthew J. Trusnovic
ALL RIGHTS RESERVED

ABSTRACT

MATTHEW J. TRUSNOVIC. Application of Local Transmission Line Modelled Metasurfaces and Comparison to Huygens-Fresnel Principle Modelled Metasurfaces.
(Under the direction of DR. KATHRYN WELDON)

Metasurfaces have many applications, from beam steering effects to polarization control. There are two main theories that are used in the creation of modern metasurfaces, one based on the Huygens-Fresnel Principle and one based on Local Transmission Line models of the metasurface. The Local Transmission Line model is the more commonly used theory, but comparing structures constructed using this method to metasurfaces created using the Huygens-Fresnel principle will show the advantages and disadvantages to each design theory.

The Huygens-Fresnel Principle modeled metasurfaces operate on the principle of a dual dipole radiation which is powered by an incident wave. The dual dipoles, electric and magnetic, radiate energy forward and backward from the surface which constructively and destructively interfere with one another. This interference creates the output wavefront as well as backward propagating waves. The metasurface is constructed of various unit cells which contain electric and magnetic dipoles, which are matched to the required transmission coefficient phase and magnitude. If this matching is not perfect, then significant backward radiation can occur and cause errors. Despite this, the output wavefront can be steering in extreme steering angles and with unique behaviour if done correctly.

The Local Transmission Line modelled surfaces operate with generalized Snell's Law at its core, which allows the metasurface to guide and transform the incident wave. The metasurface is modelled as a series of admittance blocks on a transmission line, with length of transmission line that correspond to dielectric layers between the admittance layers. The metasurface is also designed to operate multiple input modes simultaneously, allowing for the steering of TE and TM waves at different

angles using the same structure. This application is impossible for Huygens-Fresnel modelled surfaces as that theory requires different surface configurations for each operating mode, requiring the dipoles to be oriented normally to the input electric field. However, the Local Transmission Line modeled surfaces decrease in overall length as the desired steering angle increases, which decreases the accuracy of the surface for larger steering angles.

Overall, Local Transmission Line modeled metasurfaces have far more application and versatility when compared to metasurfaces designed using the Huygens-Fresnel principle. Although extreme steering angles and unique wave behaviour can be designed using the Huygens-Fresnel principle, the disadvantages in designing such a surface and the errors caused by improper matching of unit cells make this method less versatile. The Local Transmission Line theory requires a less rigorous design process for creating unit cells, and there is room for some error in the admittances that do not compromise the basic functionality of the structure. This theory also lends itself to easier design, as these surfaces can be created directly on dielectrics using current PCB technology.

ACKNOWLEDGEMENTS

This thesis would not be possible without the massive amounts of help and support I have been given throughout my academic career.

I would like to thank my advisor Dr. Kathryn Smith for all of the support and help during my graduate school journey. I would never have gotten into this field and done this with my life if she had not helped.

I would also like to thank my committee members Dr. Mario Mencagli and Dr. Edward Stokes for their critiques and time to help me complete this thesis.

I would like to also thank my friend and lab mate Kristy Hecht for her help over the years in school and research, critiquing me and helping me improve my academic self.

Finally, I would like to thank my family for always being there to support me and my dreams, wherever they take me. They have been a rock in my life and I would never be who I am today, or this far in my studies, without the endless amount of support they have given me.

TABLE OF CONTENTS

LIST OF TABLES	vii
LIST OF FIGURES	viii
CHAPTER 1: Introduction	1
1.1. Motivation	1
1.2. Topical Overview of Thesis	2
CHAPTER 2: Background	4
2.1. Overview of Electromagnetic Waves	4
2.2. Basics of Metamaterials	8
2.2.1. Types of Metamaterials	8
2.2.2. Metasurfaces	16
CHAPTER 3: Useful Design Concepts	18
3.1. Impedance	18
3.2. Floquet Theory	19
CHAPTER 4: Huygens-Fresnel Principle	24
CHAPTER 5: Transmission Line Model	40
5.1. Derivation	40
5.2. Design	46
CHAPTER 6: Conclusions	58
REFERENCES	62

LIST OF TABLES

TABLE 4.1: Positions of unit cells on metasurface and their required phase.	38
TABLE 5.1: Comparison of refraction angle to the total length of the metasurface and the number of unit cells per structural period	57

LIST OF FIGURES

FIGURE 2.1: Three different polarization states for an electromagnetic wave; a) Linear polarization, b) Elliptical polarization, c) Circular polarization	6
FIGURE 2.2: Two different operational modes of an incident wave; a) TE mode, b) TM mode	7
FIGURE 2.3: Thermal cloaking shown in [1]	10
FIGURE 2.4: Thermal cloaking shown in [2]	10
FIGURE 2.5: Device which creates a negative phase velocity effect on acoustic waves from [3]	11
FIGURE 2.6: Periodic structure that shows a negative permeability at high frequencies [4]	13
FIGURE 2.7: Permeability response of the geometry shown in Fig. 2.6 as frequency changes [4]	13
FIGURE 2.8: Geometry of the left handed metamaterial created in [5]	14
FIGURE 2.9: Dispersion curve of the a structure like the one shown in Fig. 2.8 [4]	15
FIGURE 4.1: Surface Equivalence Principle for an arbitrary close surface	26
FIGURE 4.2: Surface Equivalence Principle for an infinitely long surface	27
FIGURE 4.3: Unit cell testing simulation's geometry for a Huygens' metasurface.	33
FIGURE 4.4: Orientation of a generic unit cell geometry for a y-polarized electric field of an incoming wave.	35
FIGURE 4.5: Two different Huygens' metasurfaces used in [6] for a) a TE polarized wave and b) a TM polarized wave	35
FIGURE 4.6: Surface Impedance across the surface of the metasurface.	36
FIGURE 4.7: Surface Admittance across the surface of the metasurface.	36

FIGURE 4.8: Electromagnetic coupling coefficient across the surface of the metasurface.	36
FIGURE 4.9: Magnitude of the transmission coefficient across the surface.	37
FIGURE 4.10: Phase of the transmission coefficient across the surface.	37
FIGURE 4.11: Near field radiation for the metasurfaces proposed in [6] for a) a TE polarized wave and b) a TM polarized wave	39
FIGURE 5.1: Approximate transmission line model for the metasurface	42
FIGURE 5.2: Ideal Admittance profiles for a 20° shift in the x-polarization and 30° in the y-polarization for Y_1	45
FIGURE 5.3: Ideal Admittance profiles for a 20° shift in the x-polarization and 30° in the y-polarization for Y_2	45
FIGURE 5.4: Ideal Admittance profile for Y_1	47
FIGURE 5.5: Ideal Admittance profile for Y_2	47
FIGURE 5.6: Geometry of the chosen unit cell for the layers of the metasurface	51
FIGURE 5.7: Admittance of the unit cell shown in Fig. 5.6 as the flange length is swept	51
FIGURE 5.8: Admittance of the unit cell compared to the ideal admittance profile of the outside surface for the TE polarized wave steered at 30°	52
FIGURE 5.9: Admittance of the unit cell compared to the ideal admittance profile of the inside surface for the TE polarized wave steered at 30°	53
FIGURE 5.10: Admittance of the unit cell compared to the ideal admittance profile of the outside surface for the TM polarized wave steered at 20°	53
FIGURE 5.11: Admittance of the unit cell compared to the ideal admittance profile of the inside surface for the TM polarized wave steered at 20°	54

- FIGURE 5.12: Close up on one period of the metasurface constructed in Cmsol 55
- FIGURE 5.13: Near electric field response for the metasurface designed to steer 20° when excited with a TE Gaussian beam 56
- FIGURE 5.14: Near electric field response for the metasurface designed to steer 30° when excited with a TM Gaussian beam 56

CHAPTER 1: Introduction

1.1 Motivation

In modern society, many aspects of technology are being pushed to become electromagnetically wireless for both convenience and efficiency. This includes common place things such as high speed Wi-Fi and cellular technology, to more technologically advanced applications such as satellite technology and space travel. As such, the desire to create more dynamic and compact electromagnetic devices grows with each passing year. Most of these devices use antennas and electromagnetic structures that are composed of materials which are naturally found, or which are created as homogeneous mixtures of preexisting materials. These materials work well enough for many applications, but the limit at which these can be used for future devices is fast approaching. Antennas that are required to operate at high frequencies become physically tiny using traditional antenna design, and devices that are required to operate over large ranges of frequencies can become spatially complex and impractical to fabricate. To overcome these problems, special structures known as metamaterials can be used.

Metamaterials have the potential to create regions where the electromagnetic response of the structure acts as a material with designed properties not found in the natural world. These properties can be things such as an altered permittivity and permeability, varying wave speeds, and even a beam steering effect. With the advent of metamaterials, wireless applications can become more efficient and diverse to keep up with societal demands. These materials have a drawback however, in that metamaterials are generally three dimensional objects and as such occupy a large amount of space. An offshoot of metamaterials can solve this problem for applications in-

volving the control of electromagnetic waves, known as metasurfaces. These devices are structures that are small enough compared to the incoming wave that they are essentially two dimensional boundaries in space which can instantaneously change electromagnetic waves. There are several methods in which these metasurfaces can be created, such as using a Local Transmission Line theory and the other less intuitive methods using the Huygens-Fresnel principle as its basis. This thesis will go through the design process of using the Local Transmission Line model theory for the production of a beam steering metasurface, as well as compare it to a metasurface designed using the Huygens-Fresnel principle as its basis. The factors by which the transmission line model is more advantageous will be discussed, as well as applications in which these types of metasurface may be applied to.

1.2 Topical Overview of Thesis

This thesis will first cover general background material needed to have a basic understanding of how electromagnetic (EM) waves operate and several key characteristics by which EM waves operate. These concepts include things such as the method by which waves are defined, wave operational modes, and polarization types. Material characteristics are then discussed as well as how materials interact with propagating waves. From there, an outline on the basics of materials is described as well as an introduction to the concept of metamaterials. Different types of metamaterials are then discussed, including thermal, acoustic, and electromagnetic. As a special category of electromagnetic metamaterials, the concept of metasurfaces is introduced. The idea of metasurfaces is expanded upon as well as their application in electromagnetic wave interactions for the two different design theories: Local Transmission Line and Huygens-Fresnel theories.

Following the background information, the derivations for essential concepts needed for the testing of the metasurfaces is discussed, such as impedance and Floquet Analysis. These concepts will be defined and their utility with respect to metasurface

design will be discussed.

After the design concepts that are common between the two design methods are discussed, the design of Huygens-Fresnel theory based metasurfaces will be discussed. The basic concept and foundational theories behind this approach are covered. The theory is then applied to the application of a two dimensional surface and the scattering parameters of the surface are defined for the electric and magnetic dipoles required for the theory to be valid.

Next, the process to create the local transmission line modelled metasurface will be started. First the local transmission line model is created to simulate the interaction between the incoming wave and the metasurface. The desired phase shift for the outgoing wave is then defined and the required admittance profiles needed to create this shift are found using the transmission line model. The size of the surface is also adjusted to allow for a single period of admittance to appear across it, and the ideal admittance profile to create the phase shift is discretized to allow for allocation of unit cells. Individual unit cells that, when combined, create a profile of admittance that simulates the ideal admittance profile are then created and assigned to the metasurface structure. From there, the structure is tested in Ansys' High-Frequency Structure Software (HFSS) to verify its operation.

We conclude with a comparison of the two separate design methodologies, and a thorough discussion of the advantages and disadvantages of each method. Applications in which the two design theories excel are also separately discussed, showing where and how each method is viable.

CHAPTER 2: Background

2.1 Overview of Electromagnetic Waves

Electric and magnetic fields travel through space through a phenomenon known as electromagnetic radiation. This propagation is characterized by a simultaneous oscillation of both the electric and magnetic fields, which is commonly known as a wave. These coupled fields can be described as waves when they satisfy a second order differential equation with respect to space and time, known as a wave equation. This equation can be represented with currents and charges, known as sources, or for homogeneous regions with no currents and charges. The wave equations in homogeneous regions are largely used in calculations of waves since many natural materials do not contain wave generating currents and charges. For this derivation, the sourceless wave equations are used. These equations represent how the fields change as time advances and as the wave travels through space. Both the electric and magnetic fields must satisfy these equations, which can be seen below in Eq. 2.1 and Eq. 2.2 [7]

$$(\nabla^2 - \omega^2 \mu \epsilon) \bar{E} = 0 \quad (2.1)$$

$$(\nabla^2 - \omega^2 \mu \epsilon) \bar{B} = 0 \quad (2.2)$$

In Eq. 2.1 and Eq. 2.1, \bar{E} is the electric field, \bar{B} is the magnetic flux density, ω is the angular frequency, μ is the magnetic permeability, and ϵ is the electric permittivity. These two equations are derived using Maxwell's Equations which, along with the Lorentz force, characterize modern electromagnetics. Since it was defined that these fields are oscillating in a synchronistic manner, a frequency at which the fields oscillate

can be defined as f . This frequency is a measure of how many cycles of the fields occur within one second, measured in Hertz (Hz), and can be measured as an angular frequency $\omega = 2\pi f$. The partial spatial derivative in Eq. 2.1 and Eq. 2.2 is represented as the vector Laplacian operator ∇^2 , which is the divergence of the gradient of a function for a given space [8].

Writing the wave equations with respect to the phasor forms of the electric and magnetic field, the wave equations can be defined as the Helmholtz equations for electric and magnetic fields. These equations can be seen in Eq. 2.3 and Eq. 2.4 [7].

$$\nabla^2 \bar{E} + \omega^2 \mu \epsilon \bar{E} = 0 \quad (2.3)$$

$$\nabla^2 \bar{H} + \omega^2 \mu \epsilon \bar{H} = 0 \quad (2.4)$$

In Eq. 2.4, \bar{H} represents the magnetic field, and was converted from \bar{B} in order to have the equation have the same form as Eq. 2.3. Electromagnetic waves can oscillate in a variety of different ways, known the polarizations. These polarizations describe how the electric field of a wave changes with respect to time, and are named after the shape that is ‘traced’ by the electric field on a plane of space perpendicular to the direction of propagation as time passes. There are three polarization states that electromagnetic waves can be characterized as, linear, elliptical, and circular. Illustrations of each of these polarizations can be seen in Fig. 2.1.

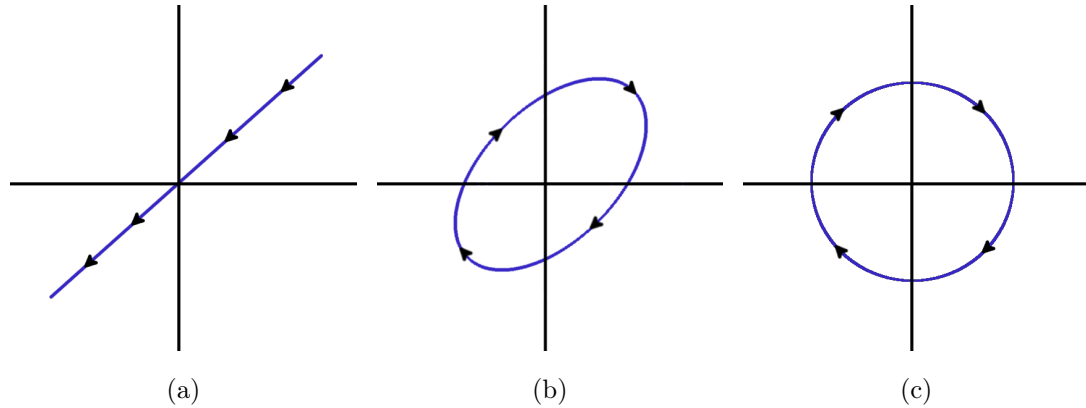


Figure 2.1: Three different polarization states for an electromagnetic wave; a) Linear polarization, b) Elliptical polarization, c) Circular polarization

Electromagnetic waves can also have several operational modes that are defined relative to the space around them. These modes are known as Transverse Electric (TE), Transverse Magnetic (TM), and Transverse Electromagnetic (TEM) waves. These different modes are defined by how the electric and magnetic fields are oriented with respect to the surrounding space and structures. For example, a wave that is incident to a surface is known to be have a TE orientation when the entire electric field is tangential to the incident surface. In the same situation, a wave is considered to be TM when the magnetic field is tangential to the incident surface. Finally, a wave is defined to be TEM when the electric and magnetic fields are tangent to the incident surface. An example showing TE and TM mode propagation can be seen in Fig. 2.2.

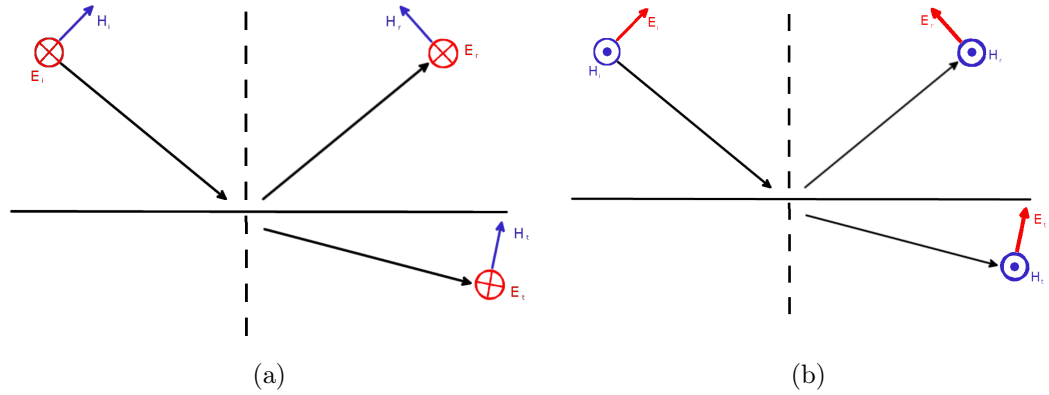


Figure 2.2: Two different operational modes of an incident wave; a) TE mode, b) TM mode

Attached to the spatial derivative component of the wave equations is the phase velocity of the propagating wave, denoted as v_p . This phase velocity is a measure of the rate at which a wave of a certain frequency travels through materials, with the electric and magnetic properties of the materials determining this velocity. As such, the phase velocity can be defined purely with respect to the electromagnetic characteristics of the material in which the wave is travelling. The electric response of the material is known as the electric permittivity, given by $\epsilon = \epsilon_r \epsilon_0$ where ϵ_r is the relative permittivity of the material and $\epsilon_0 = 8.85 \times 10^{-12}$ is the vacuum permittivity, and the magnetic response of the material is given by the magnetic permeability, shown as $\mu = \mu_r \mu_0$ where μ_r is the relative permeability of the material and $\mu_0 = 4\pi \times 10^{-7}$ is the vacuum permeability. The material properties are simply factors which scale the vacuum permittivity (ϵ_0) and permeability (μ_0) relative to the material. These relative factors can vary with time, space, frequency, as well as being tensorial with respect to the incoming wave. Most materials do not exhibit such behaviour, being classified as isotropic materials, but materials which have a tensorial behaviour that contributes to its relative permittivity and permeability are known as anisotropic materials. This anisotropic behaviour can come about due to factors such as the physical structure of the material, the number of free electrons in the material,

as well as many other factors.

2.2 Basics of Metamaterials

The basis of all engineering starts with manipulating materials into useful applications for specific problems. This may involve applications such as using wood to create a boat, using copper to transmit electricity, or even using steel to create probes for deep space missions. For most of human history, the list of materials that were available for use were limited to what was naturally found in our environment. Later on we learned how to mix different materials together to create a new material, including mixing metals to create new metals and incorporating beams into concrete. These new techniques of compiling existing materials has led to a vastly larger pool of materials at our collective disposal. This trend continues to advance, but a new concept has recently started to appear which offers a variety of new applications similar to the introduction of mixed materials compared to natural materials. This new concept is known as metamaterials, which involves creating periodic structures of mixed materials that operate outside of the normal characteristics of its constituent materials. The word metamaterial itself explains what it is, as ‘meta’ in Greek means ‘beyond’ [9], which implies that this new concept creates materials which are beyond what was capable before. There are several varieties of these metamaterials including thermal, acoustic, and electromagnetic.

2.2.1 Types of Metamaterials

The concept of metamaterials has been applied to a variety of different fields, including thermal dynamics, acoustics, and electromagnetics. In each of these fields, the desired effects from the metamaterial structures is due to the geometry, size, orientation, and spacing with respect to the constituent materials from which the structures are created. Each application uses metamaterials for different purposes and each field has different methods for creating varying effects.

2.2.1.1 Thermal Metamaterials

The main characteristic of interest for thermal metamaterials is the thermal conductivity of said materials. This is usually done through the use of laminates, which are defined as layered materials that are constructed of alternating materials of different thermal conductivities [10]. These laminates take advantage of the second law of thermodynamics, which states that the entropy of a closed system does not increase for reversible processes but increases for instantaneous processes. This law does not take into account the process by which this entropy can increase, so the laminate materials take advantage of this by shaping the entropy response in time and space [10]. As a result these new materials can be designed to create anisometric materials, redirecting thermal energy in a certain direction more than other directions, or even create thermal cloaking. Examples of anisometric thermal materials are given in [11, 12, 13]. These laminates can also be used to create thermal cloaking by controlling the direction of the heat flux, as shown in [14]. In this paper, cloaking is achieved by creating an environment of perfect insulation around the desired cloaking region as well as directing the heat flux around the region as well. Other examples of thermal cloaking are shown in [1, 15], where similar concepts are used. The experiment showing the concept of thermal cloaking in [1] can be seen in Fig. 2.3

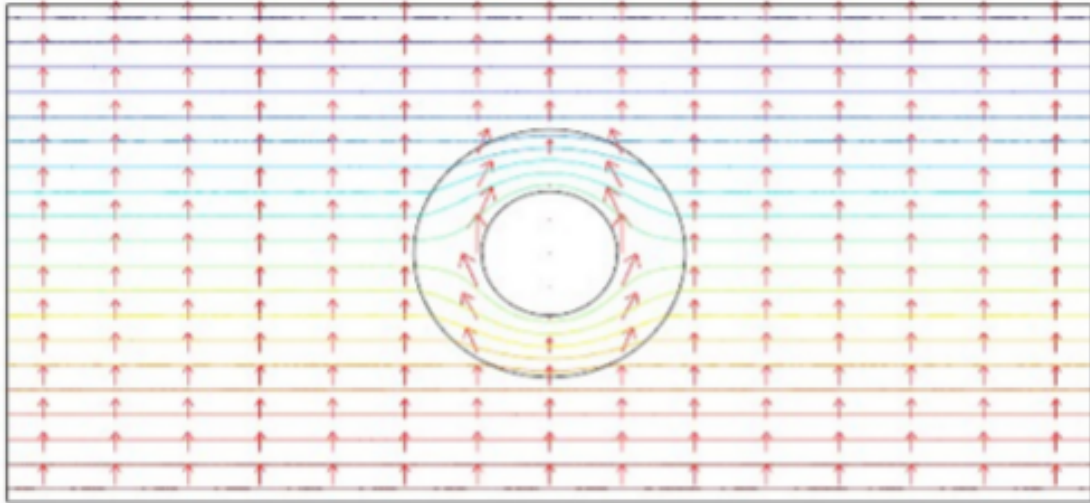


Figure 2.3: Thermal cloaking shown in [1]

Focusing of thermal energy is also possible through the use of metamaterials utilizing laminates. This focusing can involve concentrating the energy into a specific region, or even inverting the thermal energy in certain regions. This inversion is done through twisting many layers of a laminate material, creating a spiral effect of the thermal energy. This behaviour can be seen from [2] in Fig. 2.4.

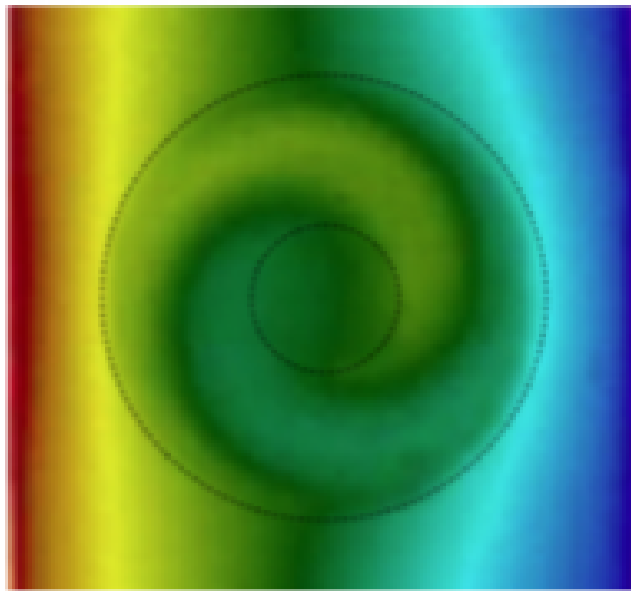


Figure 2.4: Thermal cloaking shown in [2]

2.2.1.2 Acoustic Metamaterials

Acoustic metamaterials face a different problem from most other types of metamaterials, that being the need for a medium needed for wave transfer. Since acoustic metamaterials deal with pressure waves, different considerations must be made when designing acoustic materials. Despite these limitations, acoustic metamaterials can create effects of negative phase velocity [16, 17], as well as effective acoustic cloaking [18]. These effects can be achieved via mapping these materials with varying phase velocities onto inhomogeneous and anisometric materials to create the desired cloaking effects. Similarly to the double negative permittivity and permeability metamaterials shown in the next section, acoustic metamaterials can have a double negative bulk modulus and mass density. This double negative behaviour can lead to a negative phase velocity for acoustic waves [3]. An example of a structure that exhibits this behaviour can be seen in Fig. 2.5

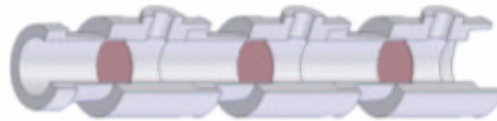


Figure 2.5: Device which creates a negative phase velocity effect on acoustic waves from [3]

The combination of membranes and holes present in the structure shown in Fig. 2.5 creates the negative phase velocity effect for different frequencies, allowing wave propagation from one end of the pipe to the other end when above a certain designed for frequency. There have also been advances in the region of semi-two dimensional acoustic metamaterials, which can generate an effective negative bulk modulus [19]. This effect was achieved through a series of closely located holes along a subwavelength thin waveguide.

2.2.1.3 Electromagnetic Metamaterials

Electromagnetic metamaterials are mainly used to control different parameters of electromagnetic wave propagation such as phase velocity, wave polarization, and varying permittivity and permeability of materials. The original goal of many early electromagnetic metamaterials was to create materials that have both negative permittivity and negative permeability. These two quantities represent the measure of the electric polarizability and magnetization of a specific material. In other words, these two variables represent how electromagnetic fields travel through a medium and explain certain properties of these traveling waves as well. The first theorization behind making these properties a negative value was done by Veselago [20] in 1968. He theorized that it may be possible to create a material that has simultaneously negative permittivity and permeability values. This situation led to the derivation of so called 'Left-handed' materials, which are named for their opposite calculation of propagation from conventional materials and their 'Right Hand Rule'. From this initial definition, several conclusions can be drawn from these left handed materials, including a negative refractive index and a reverse Doppler effect. At the time this theory was left untested as there were no realizable materials that possessed both a negative permeability and permittivity.

Materials with a negative permeability were possible, such as certain plasmas, but materials with a negative permittivity were not feasible. This changed in 1999 when Pendry et.al published a work that showed a bulk material that had an effective negative permittivity [4]. This paper showed that for a certain geometry placed in a periodic structure, an effective negative permeability can be found at high frequencies. This structure is now known as a split ring resonator and can be seen in Fig. 2.6, along with the permeability response as frequency changes in Fig. 2.7.

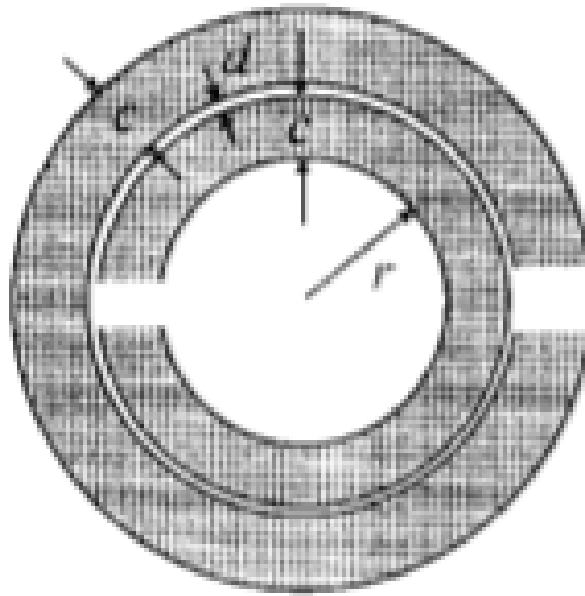


Figure 2.6: Periodic structure that shows a negative permeability at high frequencies [4]

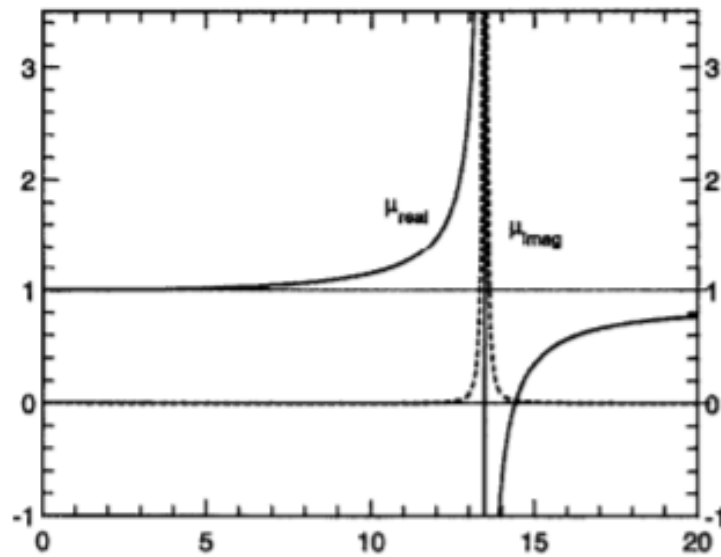


Figure 2.7: Permeability response of the geometry shown in Fig. 2.6 as frequency changes [4]

It can be seen in Fig. 2.7 that there is a resonant response in the periodic structure at around 13.5GHz, and that it is directly after this resonant point that the structure

shows a negative permeability behaviour. This is due to the ratio of capacitive coupling and inductive response at this specific frequency that this behaviour occurs. It is important to note that the incident electric field has to be parallel to the plane of the structure for this response to be valid, any other polarization of the incident field will not give the same effect. Now negative permeability materials exist, but a pure left handed material had not been achieved yet. This final breakthrough happened in 2000 in [21], where a combination of periodic split ring resonators and straight wires created a region in which both parameters were negative. This combination of resonators was designed by [5] and can be seen practically built in Fig. 2.8, and shows that the split ring resonators and wire arrays are printed on either side of a dielectric material. The dispersion curve for a structure like this can be seen in Fig. 2.9, where the solid lines is the response of the split rings alone, with the dotted lines representing the combined response of the resonators and the wire array. It can be seen that from this dispersion that the combined response bridges the previously forbidden frequency range in the response, which is due to the double negative behaviour of the structure.

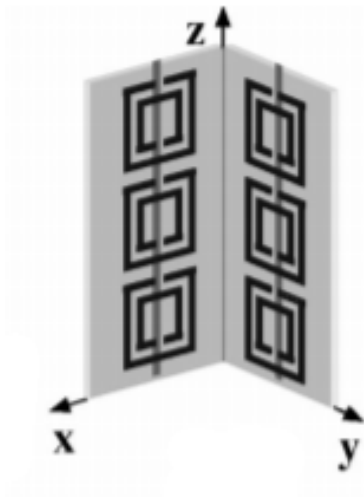


Figure 2.8: Geometry of the left handed metamaterial created in [5]

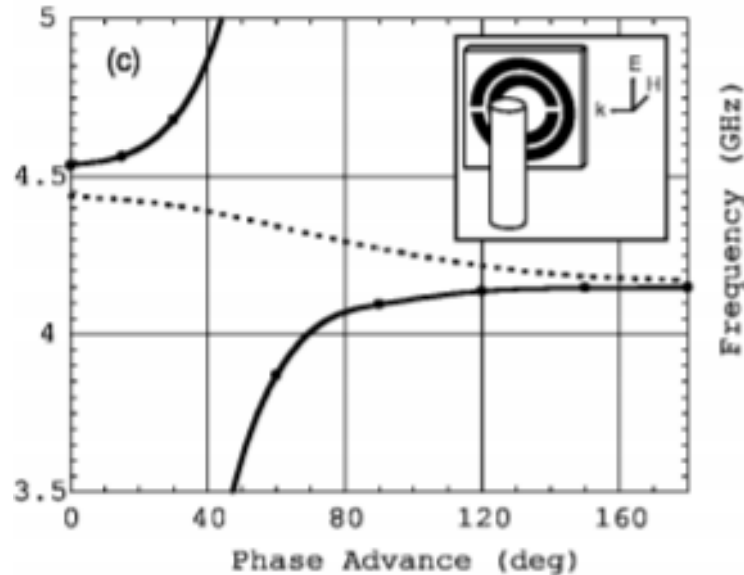


Figure 2.9: Dispersion curve of the a structure like the one shown in Fig. 2.8 [4]

After this design that showed that an approximate left handed material was created, many more metamaterial structures have been created. Most of these three dimensional structures were designed to create a negative refractive index, as shown possible in [21]. Applications using this technology for cloaking purposes is a widely researched topic, as the negative refractive index could be combined with materials that are characterized by a positive refractive index to create a cloaked region. The drawbacks of using three dimensional materials for applications such as this become more apparent now, including the overall bulkiness of three dimensional materials. A combination of a multitude of elements must be placed in a large array to exhibit the desired response, and this consumes considerable space and resources to create the total structure. The physical size of each of the components that make up the larger total structure become extremely small as the operating frequency increases, as each of the elements must have a size that is sufficiently subwavelength. The extremely small wavelength of high frequency signals necessitates the very small filaments and precise unit cell elements, which can be near impossible to fabricate accurately. A solution to this problem is to create two dimensional metamaterials, which are known

as metasurfaces. These metasurfaces have a thickness which are sufficiently subwavelength, so they approximate to a sudden boundary in space with respect to an incident wave. Since these materials are essentially just boundaries, the effective permittivity and permeability are not useful. Instead, the boundaries' impedance, transmission, and reflection are studied to affect incoming waves in a desirable manner.

2.2.2 Metasurfaces

Electromagnetic metasurfaces have several advantages when compared to three dimensional metamaterials. The two dimensional surfaces have negligible loss since they are of a subwavelength thickness compared to the incoming wave, as opposed to a bulky three dimensional material where the losses within the material are a concern. Another advantage is the overall size of the structure, as a planar metasurface takes up less space than a whole metamaterial structure. The lessened size allows metasurfaces to be more cost effective to fabricate when compared to conventional metamaterial structures. Metasurfaces also deal with the reflection, transmission, and impedance at the boundary as opposed to controlling the refractive index of a material directly. This different approach to design presents its own challenges and design techniques when compared to other metamaterials.

There are several separate theories on how metasurfaces are designed, with two separate theories being the main topic of discussion for transmitarray metasurfaces. Transmitarray metasurfaces are defined as metasurfaces that deal with the transmission of a desired incoming wave, as opposed to a reflectarray metasurface which focuses on controlling the reflections off of its surface. The first theory deals with transforming the incoming wave using a Local Transmission Line model. Each component in the metasurface is treated as a parallel section on a transmission line model of the whole structure. With this model of the local system, the transmission and reflection of a wave at the input of the system can be tailored to whatever is desired at the output of the model using standard transmission line analysis. The second

method of design for these metasurfaces deals with using the incoming wave as a excitation for the metasurface itself, which re-radiates additional fields on either side of the surface. These types of surfaces are known as Huygens' surfaces, after Christiaan Huygens, who created the foundations of this theory. This technique involves treating the surface as a combination of dipole sources which radiate independently from each other due to the incoming wave. By designing the dipoles carefully, a desired outgoing wave can be achieved.

This thesis will start with a basic background of electromagnetic radiation and characteristics, including the general theories needed to fully test and characterize the metasurfaces. After that, the theory and design of a metasurface designed with the local transmission line model theory will be discussed along with its results. Then a metasurface created using the Huygens' surface theory will be derived and tested. Finally, the two theories will be compared to show the advantages and disadvantages in each theory with respect to each other and the application of a beam steering effect.

CHAPTER 3: Useful Design Concepts

3.1 Impedance

Metasurface designs typically use the concept of impedance to create wave control effects. In circuit analysis, impedance is defined as the opposition of a circuit element to the flowing current present when a voltage is applied across said element. This opposition impedes the progression of current as energy flows, with generally higher currents corresponding to lower impedances. These impedances can have complex values, with the conventional representation of a complex impedance given below in Eq. 3.1.

$$Z = R + jX \tag{3.1}$$

In this equation, Z is the complex impedance, R is the real component of the impedance, known as the resistance, and X is the imaginary component of the impedance, known as the reactance. In general, the resistance of a component stays constant as the frequency of the voltage changes but the reactance tends to change. At lower frequencies and with direct current, the reactance tends to disappear for conventional circuitry components. As frequency rises, the reactance tends to become more prominent compared to the resistance. In electromagnetic waves the concept of impedance is also used, but with some slightly different connotation. In electromagnetics, the concept is known as wave impedance and is a ratio of the electric and magnetic fields tangent to the direction of propagation. Similarly to circuitry impedance, wave impedance can also be complex. This wave impedance for an arbitrary material is defined below in Eq. 3.2

$$Z = \sqrt{\frac{j\omega\mu_r\mu_0}{\sigma + j\omega\epsilon_r\epsilon_0}} \quad (3.2)$$

In this equation, Z is the wave impedance, ω is the angular frequency of the propagating wave, μ_r is the relative permeability of the material, μ_0 is the vacuum permeability, σ is the electric conductivity of the material, ϵ_r is the relative permittivity of the material, and ϵ_0 is the vacuum permittivity. In the case of nonconductive materials, that is to say materials which do not conduct electric currents well, σ can be assumed to be 0. As such, the wave impedance can be reduced to the form shown in Eq. 3.3.

$$Z = \sqrt{\frac{\mu_r\mu_0}{\epsilon_r\epsilon_0}} \quad (3.3)$$

This value can be used to find the speed at which the wave travels through a material, as well as the angle of refraction between materials, among several other uses. As such, these two concepts of impedance will be useful for creating metasurfaces.

3.2 Floquet Theory

Metasurfaces are constructed using many distinct components, which when composed together, create some desirable effect. In order to test these components, called unit cells, some method of analysis must be completed on said unit cells. For metasurface unit cell design, Floquet analysis is used as it allows for studying of individual geometries that lay on a periodic surface.

Consider an infinite, linear, one dimensional periodic system situated along the x axis, given as a function $Q(x)$ such that $Q(x) = Q(x + nP)$ where P is the period of the structure and n is any integer. Now introduce a propagating wave that intersects with the periodic structure with wave number $k = \sqrt{k_x^2 + k_y^2 + k_z^2}$. The resulting scattered wave can be defined in terms of several periods of the repeating structure with a form as such.

$$E(x_2) = E(x_1 + x_2) = E(x_1 + nPx) = E(x_1)e^{-jk_x nP} \quad (3.4)$$

In this situation, the wave is defined only in terms of the wave number with respect to the the x direction as the periodic structure is defined as only being periodic in the x direction. Eq. 3.4 can be manipulated into the following form for any general position along the x axis.

$$E(x) = E^n(x)e^{-jk_x} \quad (3.5)$$

Where $E^n(x) = E(x + nPx)$ along any position in the x axis. As can be seen from this, the field along the periodic structure is the same for any integer multiple of n . Due to the uniqueness theory from the differential equation of the incoming wave, each of the points along the periodic structure that are excited a distance of nP from each other have valid and true solutions. The only difference between the fields at the different positions along the periodic structure is the phase at each of the unique positions, as can be seen in Eq. 3.4. Due to validity of each of the unique positions along the structure, the periodic function $E^n(x)$ can be expressed as a Fourier Series.

$$E^n(x) = \sum_{m=-\infty}^{\infty} E_m^n e^{j\frac{2\pi xm}{P}} \quad (3.6)$$

The coefficient E_m^n can also be found as follows.

$$E_m^n = \frac{1}{P} \int_0^P E^n(x) e^{j\frac{2\pi xm}{P}} dx \quad (3.7)$$

By substituting Eq. 3.6 into Eq. 3.5, the scattered field can be seen to be a summation of all of the scattered fields along the periodic structure. This is shown in Eq. 3.8

$$E(x) = \sum_{m=-\infty}^{\infty} E_m^n e^{-jx(k_x - \frac{2\pi m}{P})} \quad (3.8)$$

The final direction of propagation for each of the propagating waves along the periodic structure can be defined using the wave number of the sum of the scattering waves in Eq. 3.8. This resulting wave number is defined as $k'_x = k_x - \frac{2\pi m}{P}$ for the x direction. This wave number defines the direction of propagation for the scattered waves, both transmitted and reflected.

This concept of one direction periodicity can be expanded upon for two and three dimensions, depending on the application. For the use of metasurfaces, the two dimension expansion is more useful, while for conventional metamaterials the three dimension expansion is more useful. In this derivation the two dimensional expansion is the only one fully explained as this is the property that will be used in the design.

To start the two dimensional Floquet analysis, first consider an infinite, linear, periodic, two dimensional plane normal to the z axis. This periodic structure can be represented as a function $Q(x, y)$ such that $Q(x, y) = Q(x + nP_x, y + mP_y)$, where P_x and P_y are the periods for both the x and y directions of the periodic structure. Now suppose that a wave that is dependent on x , y , and z intersects with this periodic structure, the resulting summation of the resulting fields can be expressed as such is Eq. 3.9.

$$E(x, y, z) = E^n(x, y, z) e^{-j(k_x + k_y)} \quad (3.9)$$

Similarly to the one dimensional case for the periodic structure, each of the positions on the structure has a valid wave present with a varying phase. This varying phase ultimately results in different directions of propagation for the incoming wave, as represented by the wavenumber. As a consequence of all of the unique and valid waves, the periodic function $E^n(x, y, z)$ can be expressed as the Fourier Series in

Eq. 3.10.

$$E^n(x, y, z) = \sum_{m=-\infty}^{\infty} \sum_{q=-\infty}^{\infty} E_{mq}^n e^{j\left(\frac{2\pi xm}{P_x} + \frac{2\pi yq}{P_y}\right)} \quad (3.10)$$

The coefficient of this Fourier Series can be derived as such:

$$E_{mq}^n(z) = \frac{1}{P_x P_y} \int_0^{P_x} \int_0^{P_y} E^n(x, y, z) e^{j\left(\frac{2\pi xm}{P_x} + \frac{2\pi yq}{P_y}\right)} dx dy \quad (3.11)$$

By substituting Eq. 3.10 into Eq. 3.9, the form of the scattered wave with considerations to the periodic structure can be found. This is shown in Eq. 3.12

$$E(x, y, z) = \sum_{m=-\infty}^{\infty} \sum_{q=-\infty}^{\infty} E_{mq}^n(z) e^{-j[xk'_x + yk'_y]} \quad (3.12)$$

This final equation shows two wave numbers for the x and y directions of propagation, as shown below.

$$k'_x = k_x - \frac{2\pi m}{P_x} \quad (3.13)$$

$$k'_y = k_y - \frac{2\pi q}{P_y} \quad (3.14)$$

For this periodic electric field to propagate as a wave, it needs to satisfy a wave equation to show it varies both in spatially and temporally. A general form of the wave equation for the electric field can be below in Eq. 3.15

$$\nabla^2 \bar{E} - \frac{1}{c^2} \frac{d}{dt} \bar{E} = 0 \quad (3.15)$$

Assuming that the electric field is separable with respect to its spatially varying components and its time varying components, this wave equation can be simplified to the Helmholtz equation, shown in Eq. 3.16

$$(\nabla^2 + k^2)\bar{E} = 0 \quad (3.16)$$

In order to prove that this field can propagate as a wave, the formula for the electric field in Eq. 3.12 must be inserted into Eq. 3.16. By simplifying this resulting equation down, the resulting relations in Eq. 3.17 and Eq. 3.18 can be found.

$$\sum_{m=-\infty}^{\infty} \sum_{q=-\infty}^{\infty} \left(\frac{d^2}{dz^2} E_{mq}^n(z) + k_{zmq}^2 \right) \quad (3.17)$$

$$k_z'^2 = k^2 - k_x'^2 - k_y'^2 \quad (3.18)$$

By using the relation being summed in Eq. 3.17, the following statement can be extracted. In this relation, $E_{mq0}^n(z)$ is a constant by which the resulting wave is propagating in the Z direction.

$$E_{mq}^n(z) = E_{mq0}^n(z) e^{-jk_{zmq}z} \quad (3.19)$$

This final constant can be plugged back into Eq. 3.12 to find the final form of the electric field with respect to the periodically repeating 2 dimensional structure. In this equation shown in Eq. 3.20, m and q dictate the mode of the periodic Floquet structure, which in essence is the position along the structure where the wave is incident

$$E(x, y, z) = \sum_{m=-\infty}^{\infty} \sum_{q=-\infty}^{\infty} E_{mq0}^n(z) e^{-j[xk'_x + yk'_y + zk'_z]} \quad (3.20)$$

CHAPTER 4: Huygens-Fresnel Principle

In 1690, the Dutch physicist Christiaan Huygens published his book “Treatise on Light” [22] which elaborated on his theory of light as a wave. Within this text, he proposed that at every point at which light intersects with a disturbance, a unique spherically propagating wave is generated. From the summation of each of these separate wavefronts, the total wavefront that characterizes the reflection on the disturbance is constructed. Later on in 1818 Augustin-Jean Fresnel expanded upon Huygens’ original theory by combining the original principle with his own concept of interference [23]. Fresnel’s concept of interference states that when waves of different phase interact with one another, they can interact to construct a new wave that may be larger, smaller, or equal in magnitude to the original waves. By applying the concept of superposition to the sources proposed by Huygens along with Fresnel’s interference theory, Fresnel formulated that the resulting wave front generated by a wave intersecting with a disturbance can be seen as a summation of the individual waves generated by each of the point sources.

Huygens’ derivation of this wavefront due to reflections failed to consider the cases where a wave may intersect with an aperture or corner, where diffraction occurs. This is due to Huygen’s assumption that each point at which a wave comes into contact with a disturbance, a spherical monopole is approximately generated. This concept was amended in 1991 by David Miller [24] when Miller proposed that the wavefront sources were instead better approximated as dipole sources. This change in source type allowed for the concept of diffraction to be resolved within Huygens’ original theory.

This theory holds true for any propagating wave front, but can be reformulated for

electromagnetics to create a resulting wavefront from surface currents. This concept is known as the surface equivalence principle [25]. This principle approximates fields generated by known currents inside of an arbitrary closed surface to be equivalent to electric and magnetic surface currents flowing on the outside of the closed surface. These imaginary surface currents generate the electric and magnetic fields that would be generated by the enclosed sources. This concept also holds true in the reverse case, where there are currents outside of the enclosed surface. The fields these outside sources create can then be approximated on the inside of the enclosed surface using equivalent surface currents that run along the surface of the enclosed contour. By holding both of these cases as true, a generalized formula for surface currents can be created for any arbitrary fields on either side of the surface. These arbitrary surface currents can be found by comparing the difference between the tangential components of the fields on either side of the surface, as seen in Eq. 4.1 and Eq. 4.2 and defined in Fig. 4.1

$$\overline{J}_s = \hat{a}_n \times (\overline{H}_2 - \overline{H}_1) \quad (4.1)$$

$$\overline{M}_s = -\hat{a}_n \times (\overline{E}_2 - \overline{E}_1) \quad (4.2)$$

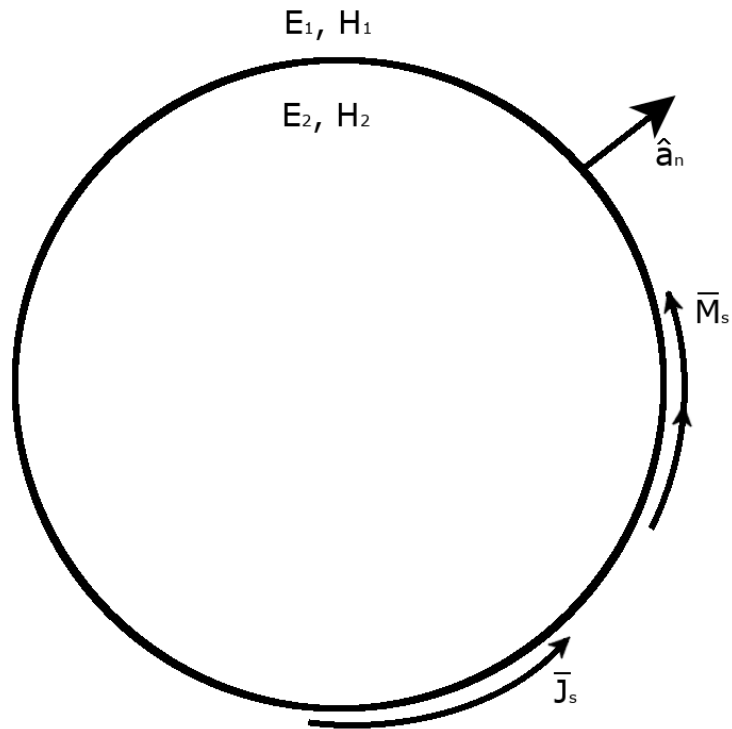


Figure 4.1: Surface Equivalence Principle for an arbitrary close surface

In Eq. 4.1 and Eq. 4.2, \bar{J}_s is the electric surface current, \bar{M}_s is the magnetic surface current, \hat{a}_n is the unit vector which is normal to the surface, \bar{E}_1 and \bar{H}_1 are the electric and magnetic fields in the first region, and \bar{E}_2 and \bar{H}_2 are the electric and magnetic fields in the second region. This general approximation for a arbitrary closed surface can be further expanded for the case of an infinite sheet. This sheet can have electric and magnetic surface currents that run along it in such a way as to approximate the field distributions on either side of the surface. These surface currents are generated in the same manner as in Eq. 4.1 and Eq. 4.2, but with a constant value for \hat{a}_n across the entire surface. This simplifies the calculation of the surface currents down to what is shown in Eq. 4.3 and Eq. 4.4 for the surface shown in Fig. 4.2.

$$\bar{\mathbf{J}}_s = \hat{\mathbf{a}}_z \times (\bar{\mathbf{H}}_2 - \bar{\mathbf{H}}_1) \quad (4.3)$$

$$\bar{\mathbf{M}}_s = -\hat{\mathbf{a}}_z \times (\bar{\mathbf{E}}_2 - \bar{\mathbf{E}}_1) \quad (4.4)$$

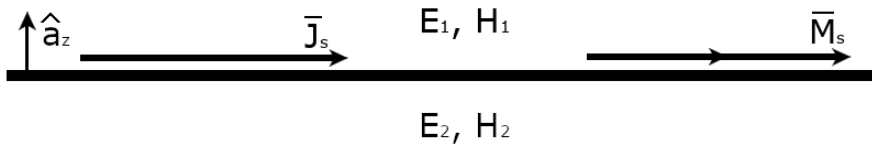


Figure 4.2: Surface Equivalence Principle for an infinitely long surface

Using this novel method of analyzing fields in space with respect to surface currents, a method to create a specific surface current in space which generates fields by itself was proposed by Eleftheriades in [26]. In this paper, he proposed using one of two methods to create these independent surface currents, either by using an array of discrete electric and magnetic dipoles, or by creating impedance and admittance surfaces. Using the electric and magnetic dipoles would create the dipole radiation that was corrected in Huygens' original theory as an incident wave came into contact with the dipoles. These dipoles would need to be made subwavelength so that the propagating waves treat the dipoles as an instantaneous surface current. These dipoles would be excited by the incoming wave, and this excitation would generate effective surface currents across the length of the dipole array. The surface currents generate fields on either side of the surface, as can be seen from the simplified version of the surface equivalence principle in Fig. 4.2. There would also be some reflected fields on the incident side of the surface, which contributes to the fields in this space. In

total on the incident side of the surface, there are the incident waves, the reflected waves, and the surface current generated waves. On the output side of the surface, there is only the transmitted incident wave as well as the surface current generated wave. Eleftheriades theorized that the dipole array would be constructed in such a way so as to have the generated waves in the incident space destructively interfere with the incident and reflected fields. The generated waves on the output end could also create a wave such that the transmitted incident wave was canceled out while still having a propagating wave.

The second approach to this concept is to create several subwavelength admittance and impedance metasurfaces which can approximate the surface current generation of the earlier mentioned dipole array. These surfaces can either be created of capacitive or inductive elements, depending on the desired output wave. Both of the mentioned methods for creating one of these Huygens' surfaces start the same way, with approximating the required total admittance and impedance needed to create the desired output wave. This can be done by evaluating the time averaged tangential components of the desired input and output waves at the surface with respect to the surface current equations given in Eq. 4.3 and Eq. 4.4. The general method for evaluating the time averaged fields on the surface is outlined in [27, 28, 29, 30]. The resulting formulation is shown below in Eq. 4.5 and Eq. 4.6.

$$\overline{E}_{t,av}|_S = \frac{1}{j\omega\overline{\alpha}_{ES}}\overline{J}_s - \overline{k}_{EM} \left(\hat{a}_n \times \overline{M}_s \right) \quad (4.5)$$

$$\overline{H}_{t,av}|_S = \frac{1}{j\omega\overline{\alpha}_{MS}}\overline{M}_s - \overline{k}_{EM} \left(\hat{a}_n \times \overline{J}_s \right) \quad (4.6)$$

In Eq. 4.5 and Eq. 4.6, $\overline{E}_{t,av}|_S$ is the time averaged electric field at the surface, $\overline{H}_{t,av}|_S$ is the time averaged magnetic field at the surface, $\overline{\alpha}_{ES}$ is the electric polarizability, $\overline{\alpha}_{MS}$ is the magnetic polarizability, and \overline{k}_{EM} is the magnetoelectric coupling

constant. In these equations the surface is assumed to be a two dimensional plane, which is not realistically possible. In order to use these equations for designing the dipole array or admittance and impedance surfaces, the total width of the elements in both cases must be subwavelength so that the incoming wave interacts with the surface as a two dimensional plane. It can also be seen that the surface currents are also tensoral, so they both vary differently in either direction that the surface occupies. This is due to the electric and magnetic polarizabilities, $\bar{\alpha}_{ES}$ and $\bar{\alpha}_{MS}$, and the magnetoelectric coupling \bar{k}_{EM} , being tensoral as well. In order to simplify the design process of the metasurface, the polarizabilities are assumed to be isometric across the surface. From this point, the admittance and impedance values needed to generate the desired surface currents can be defined as $\bar{Y}_{ES} = j\omega\bar{\alpha}_{ES}$ and $\bar{Z}_{MS} = j\omega\bar{\alpha}_{MS}$. With these definitions, Eq. 4.5 and Eq. 4.6 can be simplified to the forms given in Eq. 4.7 and Eq. 4.8.

$$\bar{E}_{t,av}|_S = \bar{Z}_{ES}\bar{J}_s - \bar{k}_{EM}(\hat{a}_z \times \bar{M}_s) \quad (4.7)$$

$$\bar{H}_{t,av}|_S = \bar{Y}_{ES}\bar{M}_s - \bar{k}_{EM}(\hat{a}_z \times \bar{J}_s) \quad (4.8)$$

These two equations are both depend on the time averaged, tangential fields at the surface, where \bar{Z}_{ES} is the surface impedance which is responsible for manipulating the magnetic field, and where \bar{Y}_{MS} is the surface admittance which is responsible for manipulating the electric field. The time averaged electric and magnetic fields can be defined as such, assuming that the surface is situated in the xy-plane.

$$\bar{E}_{t,av}|_S = \frac{1}{2}(\bar{E}_1 + \bar{E}_2)|_{z=0} \quad (4.9)$$

$$\bar{H}_{t,av}|_S = \frac{1}{2}(\bar{H}_1 + \bar{H}_2)|_{z=0} \quad (4.10)$$

From here the equations in Eq. 4.3 and Eq. 4.4 can be used with Eq. 4.7 and Eq. 4.8 to find an equation for the the surface impedance and admittance.

$$\bar{Z}_{ES} = \frac{\bar{E}_{t,av}|_S + \bar{k}_{EM} (\hat{a}_z \times \bar{J}_s)}{\hat{a}_z \times (\bar{H}_2 - \bar{H}_1)} \quad (4.11)$$

$$\bar{Y}_{MS} = \frac{\bar{H}_{t,av}|_S + \bar{k}_{EM} (\hat{a}_z \times \bar{M}_s)}{\hat{a}_z \times (\bar{E}_2 - \bar{E}_1)} \quad (4.12)$$

Since the impedance and admittance values were defined before to be purely imaginary, as well as the magnetoelectric coupling being purely real, $\Re[Z_{ES}] = \Re[Y_{MS}] = \Im[k_{EM}] = 0$, simplified versions of the impedance and admittance on the surface can be found. From here the desired input and output waves must be defined, and the incident wave is set to be normal to the surface while the output wave is directed by an arbitrary steering angle. As such, the input and output waves are defined below in Eq. 4.13, Eq. 4.14 and Eq. 4.15, Eq. 4.16 respectively.

$$\bar{E}_{in} = E_0 \hat{a}_z e^{-jkz} \quad (4.13)$$

$$\bar{H}_{in} = \frac{E_0}{\eta_0} \hat{a}_y e^{-jkz} \quad (4.14)$$

$$\bar{E}_{out} = E_0 \hat{a}_z e^{-jk(\cos(\theta_r)z + \sin(\theta_r)y)} \quad (4.15)$$

$$\bar{H}_{out} = \frac{E_0 \cos(\theta_r)}{\eta_0} \hat{a}_y e^{-jk(\cos(\theta_r)z + \sin(\theta_r)y)} \quad (4.16)$$

For Eq. 4.13, Eq. 4.14, Eq. 4.15, and Eq. 4.16, k is the incoming wave's wave number, E_0 is the magnitude of the incoming electric field, η_0 is the free space impedance, and θ_r is the outgoing steering angle. Using these defined input and output waves, the

total surface impedance and admittance can be solved for. These resulting equations can be seen in Eq. 4.17 and Eq. 4.18

$$\bar{Z}_{SE} = \frac{-j}{2} \Im \left[\frac{\bar{E}_{out} + \bar{E}_{in}}{\bar{H}_{out} - \bar{H}_{in}} \right] - j\bar{k}_{EM} \Im \left[\frac{\bar{E}_{out} - \bar{E}_{in}}{\bar{H}_{out} - \bar{H}_{in}} \right] \quad (4.17)$$

$$\bar{Y}_{SE} = \frac{-j}{2} \Im \left[\frac{\bar{H}_{out} + \bar{H}_{in}}{\bar{E}_{out} - \bar{E}_{in}} \right] + j\bar{k}_{EM} \Im \left[\frac{\bar{H}_{out} - \bar{H}_{in}}{\bar{E}_{out} - \bar{E}_{in}} \right] \quad (4.18)$$

$$\bar{k}_{EM} = \frac{\Re \left[\bar{E}_{out} \bar{H}_{in}^* - \bar{E}_{in} \bar{H}_{out}^* \right]}{2\Re \left[(\bar{E}_{out} - \bar{E}_{in}) (\bar{H}_{out} - \bar{H}_{in})^* \right]} \quad (4.19)$$

Using these two equations, the equivalent surface admittance and impedance approach to Huygen's surfaces can be used, but in order to use discrete electric and magnetic dipoles for the surface, the scattering parameters must be obtained. To do so, it is useful to first define the surface's impedance matrix. The general form for an impedance matrix is given in Eq. 4.20

$$\begin{bmatrix} E_{out} \\ E_{in} \end{bmatrix} = \begin{bmatrix} Z_{11} & Z_{12} \\ Z_{21} & Z_{22} \end{bmatrix} \begin{bmatrix} H_{out} \\ H_{in} \end{bmatrix} \quad (4.20)$$

By equating Eq. 4.20 to Eq. 4.11 and Eq. 4.12, each component of the Z matrix can be found. These resulting values can be seen below.

$$Z_{11} = Z_{ES} + \frac{(1 + 2k_{EM})^2}{4Y_{MS}} \quad (4.21)$$

$$Z_{22} = Z_{ES} + \frac{(1 - 2k_{EM})^2}{4Y_{MS}} \quad (4.22)$$

$$Z_{12} = Z_{21} = Z_{ES} + \frac{(1 + 2k_{EM})(1 - 2k_{EM})}{4Y_{MS}} \quad (4.23)$$

Using these impedance parameters of the system as a whole, the scattering parameters can be found using the conversions derived in [31]. These conversions take into account the normalized impedances on each side of the surface, shown as Z_{01} and Z_{02} . The final conversion between the impedance parameters and the scattering parameters can be seen below.

$$Z_{01} = \eta, Z_{02} = \frac{\eta}{\cos(\theta_r)} \quad (4.24)$$

$$Z_{11n} = \frac{Z_{11}}{Z_{01}}, Z_{22n} = \frac{Z_{22}}{Z_{02}} \quad (4.25)$$

$$Z_{12n} = \frac{Z_{12}}{\sqrt{Z_{01}Z_{02}}}, Z_{21n} = \frac{Z_{21}}{\sqrt{Z_{01}Z_{02}}} \quad (4.26)$$

$$S_{11} = \frac{\left(Z_{11n} - \frac{Z_{01}^*}{Z_{01}}\right)(Z_{22n+1}) - Z_{12n}Z_{21n}}{(Z_{11n+1})(Z_{22n+1}) - Z_{12n}Z_{21n}} \quad (4.27)$$

$$S_{12} = \frac{2Z_{21n}\sqrt{\frac{R_{01}R_{02}}{Z_{01}Z_{02}}}}{(Z_{11n+1})(Z_{22n+1}) - Z_{12n}Z_{21n}} \quad (4.28)$$

$$S_{21} = \frac{2Z_{12n}\sqrt{\frac{R_{01}R_{02}}{Z_{01}Z_{02}}}}{(Z_{11n+1})(Z_{22n+1}) - Z_{12n}Z_{21n}} \quad (4.29)$$

$$S_{22} = \frac{\left(Z_{22n} - \frac{Z_{02}^*}{Z_{02}}\right)(Z_{11n+1}) - Z_{12n}Z_{21n}}{(Z_{11n+1})(Z_{22n+1}) - Z_{12n}Z_{21n}} \quad (4.30)$$

In Eq. 4.24, η is the intrinsic impedance of each material, and in Eq. 4.28 and Eq. 4.29, R_{01} and R_{02} are the real portions of the intrinsic impedance in each region. For this design to work, the magnitude of the reflection coefficient (S_{11}) must be essentially 0 so that there are no total reflected fields. The magnitude of the

transmission coefficient (S_{12}) must be close to 1, and the phase of the transmission coefficient can vary. This varying phase is the property by which the screen steers the incoming beam.

From this point, testing to find appropriate unit cell designs for the structure can be done. This process is done by applying Floquet analysis to each individual unit cell in a program such as HFSS. This Floquet analysis takes the structure shown in Fig. 4.3 and periodically repeats it across an infinite plane. This process is done so that the unit cells can be tested with a coupling effect of similarly shaped neighbors, which ultimately gives the effective transmission and reflection properties of the tested unit cell. Different permutations on the size, shape, and position of each of the dipole elements need to be simulated in order to build a database upon which the appropriate geometries may be selected for their appropriate placement in the total structure.

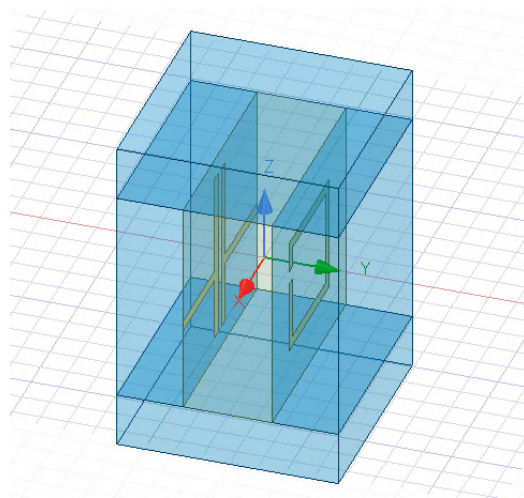


Figure 4.3: Unit cell testing simulation's geometry for a Huygens' metasurface.

As can be seen in Fig. 4.3, the entire unit cell structure, including the dielectric slab that connects the electric and magnetic dipoles, is placed between two large regions of vacuum. These vacuum regions are relatively large so that no coupling effects may occur from the input port, while the phase is de-embedded to the unit cell to allow for accurate measurements of the scattering parameters. These unit cells are sampled by

taking various measurements across the required data. For Huygens-Fresnel surfaces local periodicity does not need to be maintained for valid operation for the entire structure, so individual unit cells can vary in design. This is due to the absolute transmission and reflection being used in the design, which does not rely on a gradual of geometry to create the desired response. As such, different geometries can be used next to each other in order to create the desired steering outcome. The only limitations on this design is the fact that these unit cell designs need to operate as dipoles, either electric or magnetic, so that the desired creation behaviour is created. Several examples of this behaviour can be seen in [6, 30, 32, 33, 34]. All of these sources use various geometries of dipole structures in order to create the desired field generation on either side of the surface, creating effects from steering the incident energy to focusing the outgoing beam. As a point of comparison with the local transmission line design, a Huygens' surface that is designed for beam steering is used. This design is used so as to draw direct comparisons between the two methods, as well as weight the advantages and disadvantages against each other. To compare the local transmission line modelled metasurface, the design in [6] will be used. Several important differences between the two designs are the operational frequencies of each surface as well as the desired angle of refraction. For the Huygens' designed surface, the operational frequency is 20GHz and has a desired steering angle of 71.8° compared to the local transmission line modelled surface which has an operational frequency of 5GHz and a steering angle of either 20° or 30° .

An important distinction between the two design approaches is in the orientation and design of the individual unit cells. The Huygens' designed surface requires unit cell geometries that are oriented normal to the direction of the incident electric fields. As such, the unit cells for an incoming wave that is polarized to have the electric field purely in the x-direction must be oriented in the y-z plane, and an incoming electric field that is polarized in the y-direction must have unit cells that are normal to the

x-z plane. An example of this unit cell orientation can be seen in Fig. 4.4, where the square in the x-z plane is a generic unit cell for a y-polarized electric field.

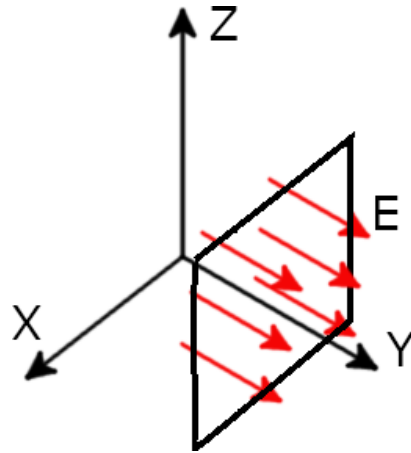


Figure 4.4: Orientation of a generic unit cell geometry for a y-polarized electric field of an incoming wave.

As such, TE and TM polarized waves are required to have separate geometries in order to create a steering effect in each direction. The metasurfaces in [6] were designed for each of these conditions in mind, with a TE and TM polarized surface being shown in Fig. 4.5

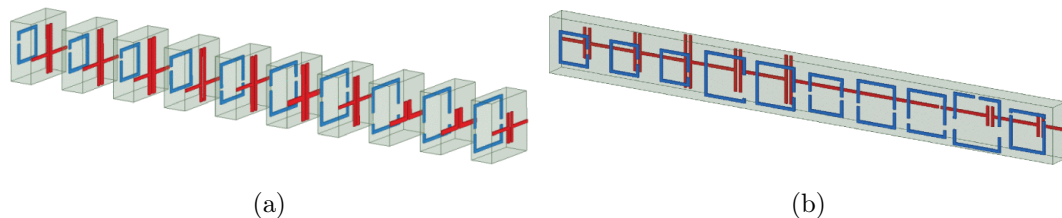


Figure 4.5: Two different Huygens' metasurfaces used in [6] for a) a TE polarized wave and b) a TM polarized wave

The individual unit cells were chosen using the theory discussed earlier in this section, starting with applying Eq. 4.17, Eq. 4.18, and Eq. 4.19 with a desired refraction angle of 71.8° and a normally incident plane wave. The resulting surface impedance, admittance, and electromagnetic coupling can be seen in Fig. 4.6, Fig. 4.7, and Fig. 4.8 respectively.

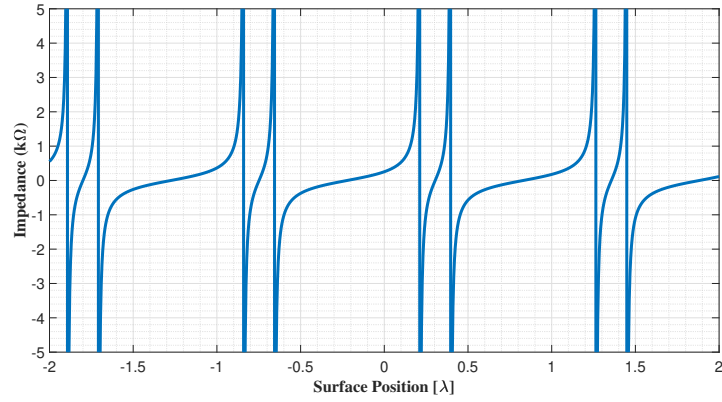


Figure 4.6: Surface Impedance across the surface of the metasurface.

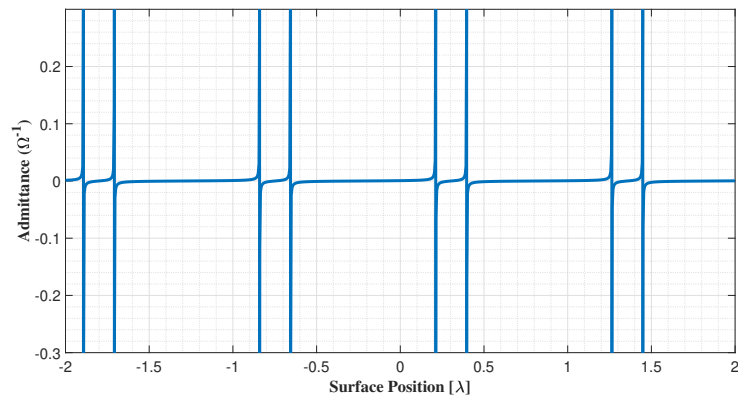


Figure 4.7: Surface Admittance across the surface of the metasurface.

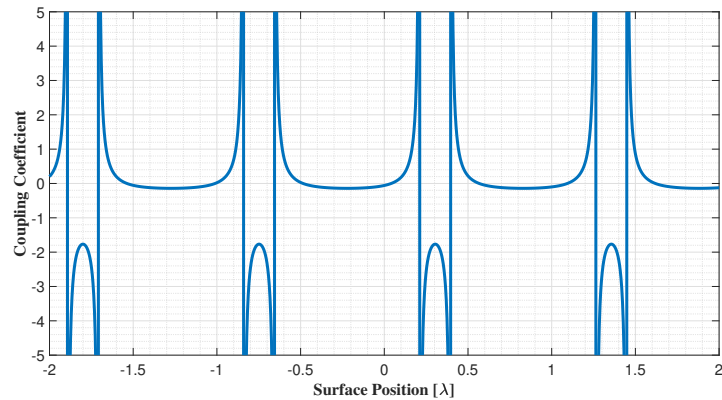


Figure 4.8: Electromagnetic coupling coefficient across the surface of the metasurface.

Now that the impedance and admittance values at the metasurface have been calcu-

lated, their values can be inserted into Eqs. 4.21, 4.22, and 4.23 to find the impedance parameters of the surface. Using these impedance parameters, the transmission parameters can be found using Eq. 4.28. This transmission coefficient is then plotted across the metasurface to ensure that there is perfect transmission and a phase gradient. The magnitude and phase of the transmission coefficient can be seen in Figs. 4.9 and 4.10 respectively.

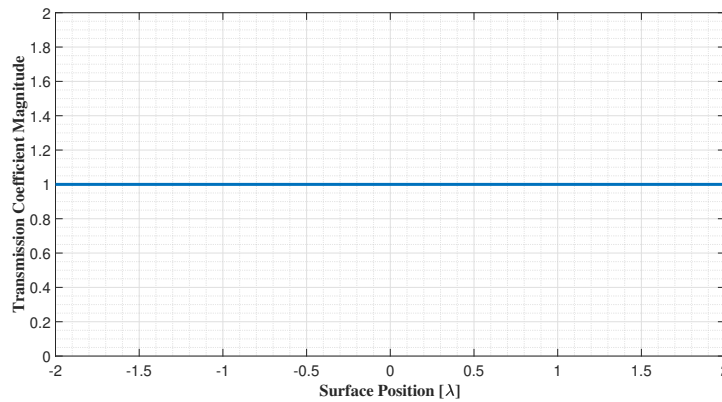


Figure 4.9: Magnitude of the transmission coefficient across the surface.

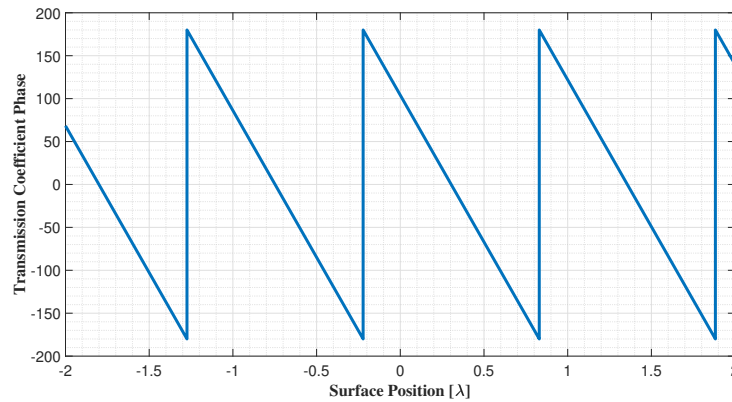


Figure 4.10: Phase of the transmission coefficient across the surface.

One period of the structure is chosen based on the phase distribution, so that only one single cycle of the phase is repeated. For this application, one period of the structure was found to be approximately 1.05λ . This period is discretized into 10 distinct points of phase, which are summarized in Table 4.1, and which results in

10 distinct unit cells that each have a size of 0.105λ . The unit cells located at the distances mentioned on this table must have their corresponding phases in order for the metasurface to operate correctly.

Table 4.1: Positions of unit cells on metasurface and their required phase.

Position (λ)	Phase Angle
-0.1694	161°
-0.0642	126°
0.0410	89°
0.1462	53°
0.2514	17°
0.3567	-18°
0.4619	-55°
0.5671	-90°
0.6723	-126°
0.7775	-162°

The testing for unit cell geometries was done by [6], and a unit cell design for each of the locations was found. The last step in this process was simply to place the unit cells next to each other and verify the surface's operation. This was done in HFSS and tested with the same setup that the local transmission line theory metasurface was tested over. The resulting field structure can be seen in Fig. 4.11. It can be seen that there are some meaningful reflections at the input of the metasurface, as well a nonideal refraction at the output of the surface. The resulting wave ends up propagating at an angle of 62° , which is 9.8° less than the desired steering angle. This discrepancy was due to the physical size of the surface. Since the surface is no infinite in nature, the limitations on the number of unit cells limits the total steering angle of the resulting wave.

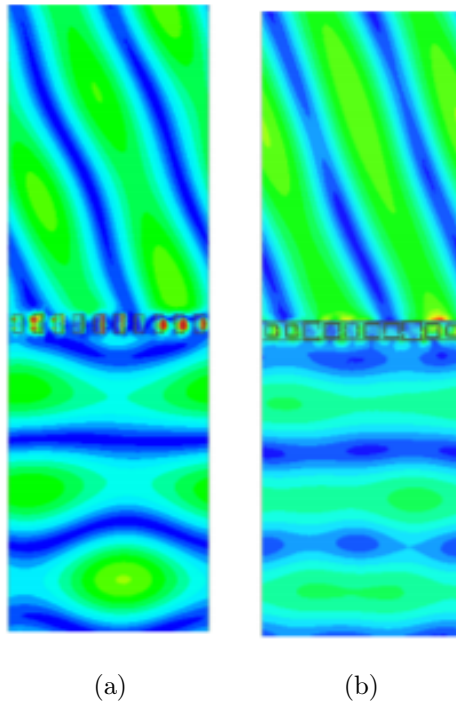


Figure 4.11: Near field radiation for the metasurfaces proposed in [6] for a) a TE polarized wave and b) a TM polarized wave

Metasurfaces designed through this method have various problems and difficulties in their design approach. Since this theory relies on the fact that the incident wave is nullified by the fields generated by the surface, any discrepancies in the generated field may result in noticeable reflections at the input. Due to this, accurate field generation at the output of the metasurface is difficult to achieve in general. Long amounts of time tend to be required to find appropriate unit cell structures that can satisfy the transmission magnitude and phase requirements, which is another major drawback to this theory. However, extreme steering angle and exotic wave behaviour is possible using this theory if accurate components are created for its operation.

CHAPTER 5: Transmission Line Model

This section deals with the derivation and design of a multi-directional metasurface based on an approximate transmission line model. This model is used to create a different impedance profile for each desired direction of phase control, which in this project involves a surface with two independent phase shifts. Each of these different directions of phase shift can have different shifts from one another, allowing for a dynamic response in the behaviour of the metasurface without changing the physical shape of the screen.

5.1 Derivation

To start approximating the metasurface as a transmission line, first the generalized Snell's Law must be used. This law states that the permittivity and phase of the first region with a phase shift relates to the permittivity and phase of the second region. This is shown in equation 5.1 [35], assuming that the phase discontinuity at the interface between the two regions varies in the x direction.

$$\sqrt{\epsilon_{r1}}\sin(\theta_i) + \frac{1}{k} \frac{\partial \Phi}{\partial x} = \sqrt{\epsilon_{r2}}\sin(\theta_r) \quad (5.1)$$

In Eq. 5.1, ϵ_{r1} and ϵ_{r2} are the relative permittivities in region 1 and 2, θ_1 and θ_2 are the steering angles of the fields in each region with relation to the normal vector of the boundary between the two regions, k is the wave number of the propagating wave, and Φ is the distribution of a phase discontinuity along the boundary. Using the holographic principle on the desired phase discontinuity in the generalized Snell's Law, the phase of the outgoing wave can be written as such. In this derivation the phase discontinuity with respect to the x direction is used.

$$\Phi_{surface} = \angle E_x - kX \sin(\theta) \quad (5.2)$$

From this equation it can be seen that the phase changes along the physical x axis, causing a gradient of the phase in that direction, assuming that $\angle E_x$ is the phase of the electric field in the direction, θ is the desired steering angle, and X is the position on the boundary in the x direction. This gradient of the phase is the driving force behind the phase control effect exhibited by the screen.

Using this principle, a three layer metasurface was chosen to be designed, the layers of the metasurface being the three interfaces between the air and the dielectric the surface is printed on, between the two dielectric layers, and between the dielectric and air. The screen was desired to have perfect transmission, no reflections, and be reciprocal. Due to the constraint of the screen to be reciprocal, the inner and outer layers of the metascreen were chosen to have the same admittance value, as the three layer design with identical outside layers have sufficient degrees of freedom to allow for these design constraints to be met [36].

From these assumptions, the entire screen can be approximated as a transmission line as shown in Fig. 5.1. This method of creating a beam steering effect with metasurfaces has been shown to be effective with high rates of transmission and low reflections [37, 38] In this model, k_{z0} is the wavenumber of the wave in air, k_{z1} is the wave number of the wave in the dielectric, Y_1 is the admittance of the outer layers of the metasurface, Y_2 is the admittance of the inner layers, Z_0 is the free space impedance for the exciting wave, and Z_1 is the impedance of the dielectric for the exciting wave.

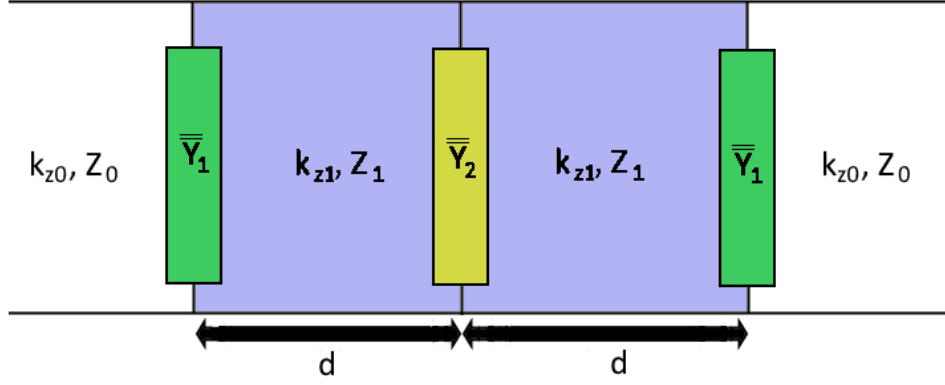


Figure 5.1: Approximate transmission line model for the metasurface

In this application k_{z0} and k_{z1} are the wave numbers of the propagating wave in air and in the dielectric, and are defined as such. k_0 is also the free space wave number of the propagating wave.

$$k_{z0} = k_0 \sqrt{1 - \sin^2(\theta_i)} \quad (5.3)$$

$$k_{z1} = k_0 \sqrt{\epsilon_r - \sin^2(\theta_i)} \quad (5.4)$$

In this application, the incoming wave is assumed to incident normal to the metasurface so θ_i is assumed to be 0. Due to this, the wave numbers can be rewritten as such.

$$k_{z0} = k_0 \quad (5.5)$$

$$k_{z1} = k_0 \sqrt{\epsilon_r} \quad (5.6)$$

Using these wavenumbers and the defined admittances and impedances, the scattering parameters of the entire transmission line can be found. To achieve this, the

ABCD matrix are defined below. The ABCD matrix for the dielectric material is given as such, assuming the dielectric materials as portions of a transmission line [7].

$$ABCD_d = \begin{bmatrix} \cos(k_{z1}d) & jZ_1 \sin(k_{z1}d) \\ j\frac{1}{Z_1} \sin(k_{z1}d) & \cos(k_{z1}d) \end{bmatrix} \quad (5.7)$$

In this equation, d is given as the thickness of the dielectric layer. The ABCD matrix for an admittance load on a transmission line is given as follows. This equation can be used for any admittance load so it is used for both the Y_1 and Y_2 values.

$$ABCD_{Y_n} = \begin{bmatrix} 1 & 0 \\ Y_n & 1 \end{bmatrix} \quad (5.8)$$

Combining each component on the transmission line involves cascading several of these ABCD matrices together, which creates the equation shown below.

$$ABCD_{total} = \begin{bmatrix} 1 & 0 \\ Y_1 & 1 \end{bmatrix} \begin{bmatrix} \cos(k_{z1}d) & jZ_1 \sin(k_{z1}d) \\ j\frac{1}{Z_1} \sin(k_{z1}d) & \cos(k_{z1}d) \end{bmatrix} \begin{bmatrix} 1 & 0 \\ Y_2 & 1 \end{bmatrix} \dots \\ \begin{bmatrix} \cos(k_{z1}d) & jZ_1 \sin(k_{z1}d) \\ j\frac{1}{Z_1} \sin(k_{z1}d) & \cos(k_{z1}d) \end{bmatrix} \begin{bmatrix} 1 & 0 \\ Y_1 & 1 \end{bmatrix} \quad (5.9)$$

This equation simplifies down to a total ABCD matrix for the entire transmission line structure. This ABCD matrix can then be transformed into its equivalent scattering parameter matrix. Due to the desire assumption that the screen will be reciprocal, the reflection coefficients, S_{11} and S_{22} , can be assumed to be equal, as well as the transmission coefficients, S_{12} and S_{21} . From this we can define the scattering parameters as shown below.

$$S_{11} = \frac{A + B/Z_0 - CZ_0 - D}{A + B/Z_0 + CZ_0 + D} \quad (5.10)$$

$$S_{12} = \frac{2(AD - BC)}{A + B/Z_0 + CZ_0 + D} \quad (5.11)$$

In Eq. 5.10 and Eq. 5.11, A , B , C , and D are all the components of the ABCD matrix given in Eq. 5.9. Since it is desired to have a metasurface that has perfect transmission and no reflections, with a phase shift imposed by the screen, the scattering parameters can be defined $S_{11} = 0$ and $S_{12} = e^{j\theta}$. From these definitions of the scattering parameters, Eq. 5.10 and Eq. 5.11 can be solved to find the equivalent admittance values for each of the surfaces in the overall structure. These resulting equations can be seen below, where θ is the desired steering angle after the metasurface.

$$Y_1 = \frac{j}{Z_1 \tan(k_{z1}d)} + \frac{j}{Z_1 \tan(\theta/2)} \quad (5.12)$$

$$Y_2 = \frac{j [Z_0 \sin(\theta/2) + Z_0 \sin(3\theta/2) + 2Z_1 \sin(2k_{z1}d) \cos(\theta/2)]}{2Z_1^2 \cos(\theta/2) \sin^2(k_{z1}d)} \quad (5.13)$$

These two equations create the ideal admittance gradients needed to steer the incoming wave in the correct direction. This data will be used to match the future unit cell designs to so as to create the same effect with the actual design as in the theoretical design. In order to create the desired effect of dual polarization beam steering, these two equations need to be applied for each polarization with their respective steering angles. The difference between two such admittance profiles can be seen in Fig. 5.2 and Fig. 5.3 for the X and Y polarizations with a steering of 20° and 30° respectively.

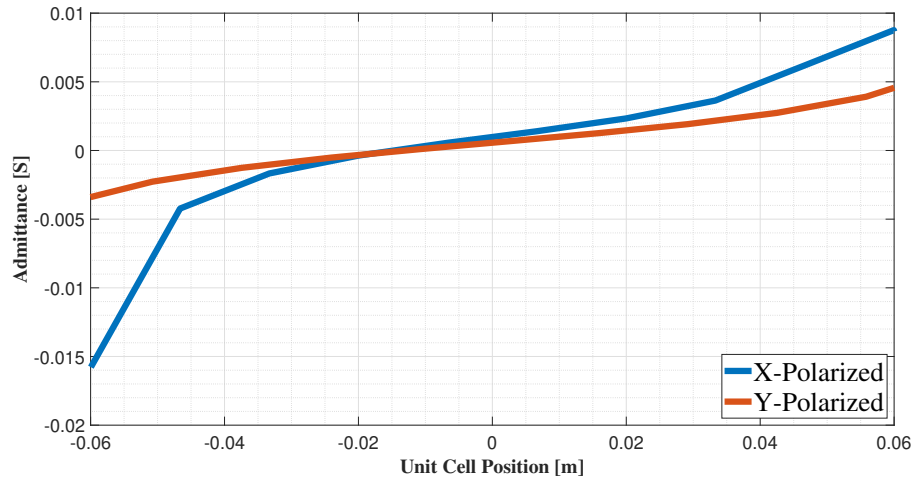


Figure 5.2: Ideal Admittance profiles for a 20° shift in the x-polarization and 30° in the y-polarization for Y_1

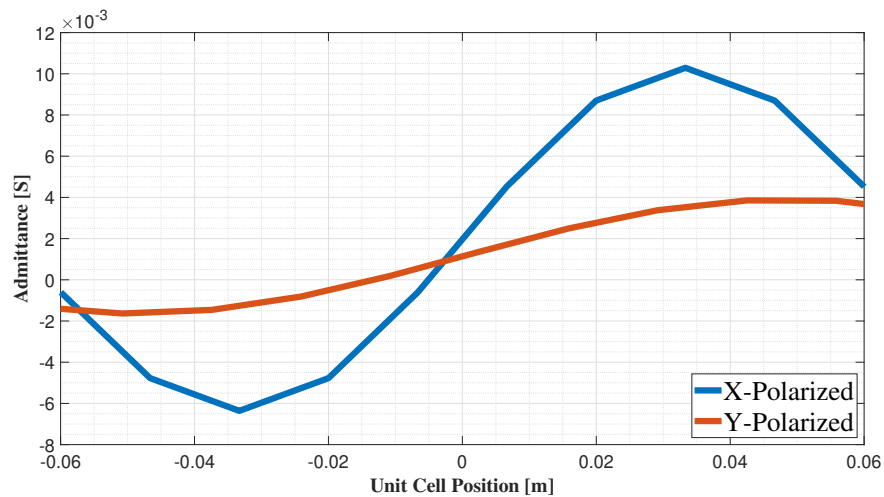


Figure 5.3: Ideal Admittance profiles for a 20° shift in the x-polarization and 30° in the y-polarization for Y_2

As it can be seen between from these two figures, the admittance profiles need to be unique for each polarization. This presents a tricky problem where a unit cell needs to be able to have a tensoral admittance that varies across the surface while still maintaining high transmission and low reflections. The unit cells must also cover the full range of phase that is needed for transmission so that proper transmission and wave controlling effects may occur [39] This hurdle was overcome by the physical

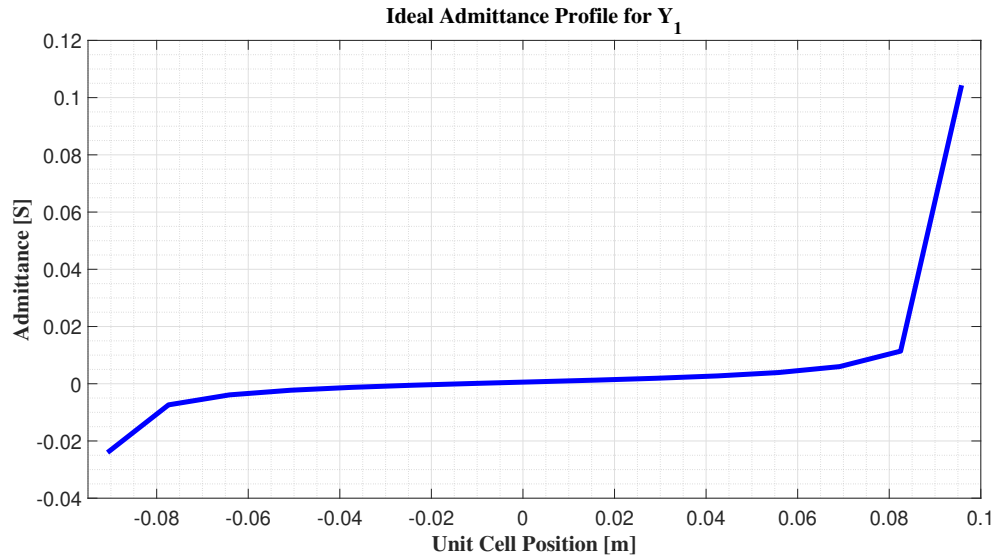
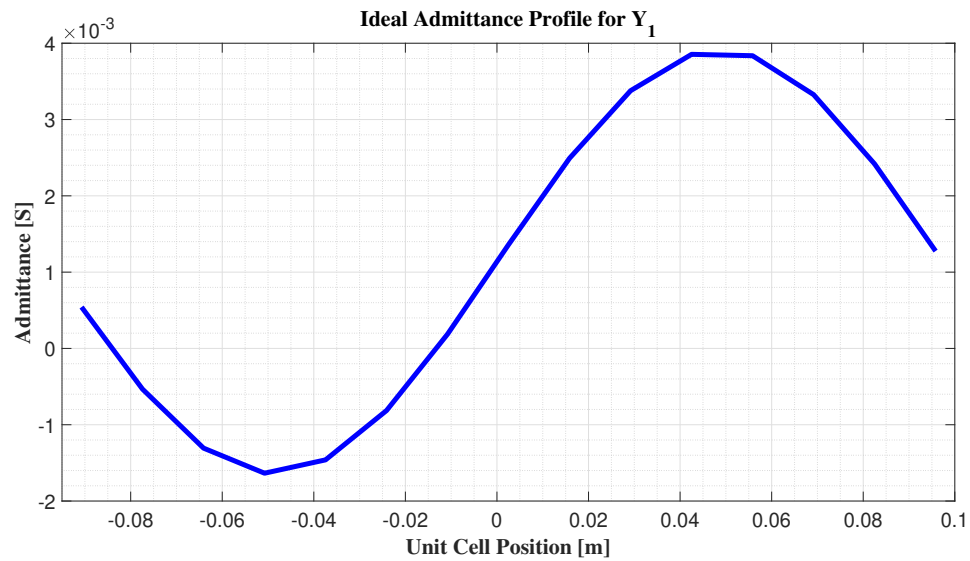
design of the unit cells, as discussed in the following section.

5.2 Design

In order to construct an actual, physically realizable metasurface, the admittance profile values as outlined in the above derivation must be constrained to a finite length that can be discretized into individual unit cell geometries. To calculate the required size of the surface, the wave length of the incoming wave is scaled by a length factor that is related to the desired resulting phase shift. The total length of a single period of the metasurface can be derived from the following equation.

$$length = \frac{\lambda}{\sin(\theta)} \quad (5.14)$$

In Eq. 5.14, λ is the wavelength of the propagating wave, and θ is the desired steering angle. Equation 5.14 keeps the total length of the screen to a size such that the phase of the admittance varies from 0 to 2π , which allows the entire incoming wave to interact with the surface. From here the entire length of the surface is split up into separate unit cells of the same size to allow for physical geometries to be placed in their position. Each of these geometries must approximate an appropriate admittance value at each of the locations in such a fashion as to recreate the originally calculated admittance profile. To achieve this, the calculated admittance profile was sampled at the center point of each unit cell location. This correlated admittance and location data will be used to choose an appropriate unit cell structure that matches the data. An example of one of these admittance profiles for an X-polarized wave steered at 20° can be seen in Fig. 5.4 for the Y_1 admittance, and in Fig. 5.5 for the Y_2 admittance.

Figure 5.4: Ideal Admittance profile for Y_1 Figure 5.5: Ideal Admittance profile for Y_2

When designing the unit cell geometries, several design considerations were taken into account. First, the principle of local periodicity was taken into account. This principle states that geometries which are in close proximity to the observed geometry will have essentially the same response if the difference between the geometries is minuscule. Using this principle, the unit cells can be designed with the same basic unit cell structure and have a single part of the geometry that changes to create the

required admittance gradient. This single varying geometric parameter must change gradually across the surface for local periodicity to hold true. As a result, surfaces that have a more gradual change in the geometric parameter will most accurately model the ideal admittance profile they are designed to match.

Another design consideration taken into account is the multiple polarization steering angles that are needed to be designed for. For each polarization, there is a different admittance profile that needs to be matched to. This means that there needs to be a separate geometric parameter for each polarization that changes each admittance within the same unit cell structure. To keep local periodicity, the structure must be symmetrical across each of the polarizations while maintaining the independence of each admittance profile.

From these design considerations, the design of appropriate unit cell geometries can be started. This testing was done in ANSYS' High Frequency Structure Simulator (HFSS) using the Driven Modal simulation. This type of simulation allows for Floquet analysis to be performed on the specified geometry within HFSS. This analysis creates an infinitely period structure of the unit cell geometry that is excited from the specified input port. This simulation type is useful when simulating unit cells assuming local periodicity of geometries, as the periodic structure of the same geometry generates the same response as the slowly changing geometries of the proposed metasurface. There were two separate simulations that were done on each proposed cell geometry, one simulation where the geometry was placed between air and the dielectric material, and one where the same geometry was placed between two slabs of the dielectric material. These two separate simulations were done to find geometries that could work for either the outside profile or the inside profile. The scattering parameters were extracted from the simulations and put through the following equations to extract the equivalent admittances of the geometry.

$$Z = Z_{0,TE/TM} \frac{1 + S_{11}}{1 - S_{11}} \quad (5.15)$$

$$Y_1^{MTs,TE/TM} = \frac{1}{Z} - Y_{1,TE/TM} \quad (5.16)$$

In Eq. 5.15, S_{11} is the reflection coefficient of the unit cell being tested. These two equations are valid for extracting the actual admittance values for the geometries appropriate for the outer admittance profiles. For this situation, $Z_{0,TE/TM}$ and $Y_{1,TE/TM}$ are defined below for the impedances and admittances for free space and the dielectric relative to the polarization of the incoming wave.

$$Z_{0,TE} = \frac{\eta_0 k_0}{k_z} \quad (5.17)$$

$$Z_{0,TM} = \frac{\eta_0 k_z}{k_0} \quad (5.18)$$

$$Z_{1,TE} = \frac{1}{Y_{1,TE}} = \frac{\eta_1 k_1}{k_{z1}} \quad (5.19)$$

$$Z_{1,TM} = \frac{1}{Y_{1,TM}} = \frac{\eta_1 k_{z1}}{k_1} \quad (5.20)$$

In these equations, η_0 and η_1 are the the characteristic impedances of free space and the dielectric, k_0 and k_1 are the wave numbers of the propagating wave in each material, and k_z and k_{z1} are the wave numbers of the propagating wave with respect to the incident angle of the incoming wave. These values are defined below where ϵ_r is the relative permittivity of the dielectric material and f is the frequency of the incoming wave.

$$\eta_0 = \sqrt{\frac{\mu_0}{\epsilon_0}} \quad (5.21)$$

$$\eta_1 = \frac{1}{\sqrt{\epsilon_r}} \quad (5.22)$$

$$k_0 = \frac{2\pi f}{c} \quad (5.23)$$

$$k_1 = k_0 \sqrt{\epsilon_r} \quad (5.24)$$

$$k_z = k_0 \sqrt{1 - \sin^2(\theta_i)} \quad (5.25)$$

$$k_{z1} = k_0 \sqrt{\epsilon_r - \sin^2(\theta_i)} \quad (5.26)$$

In this project, the incidence that was considered was normal incidence, so $k_0 = k_z$. With all of these equations in place for verifying the admittances of each layer, testing can be done on actual geometries for the unit cells. There were several different designs tested, with varying schemes for creating independence of the polarizations. Some of the proposed geometries had an outer flange that changed in length to create an varied admittance effect, while others used a changing length of the base design or cross hatching design. In the end, a modification of the traditional Jerusalem cross unit cell design was chosen for the inner and outer admittance sheets. This design can be seen in Fig. 5.6. The geometry was implemented as a slot design, so that the majority of the surface is a perfect electric conductor (PEC) and with periodic cutouts in the shape of this unit cell. The length of the flanges were swept to vary the admittance in each direction such that the admittance in the x-direction was effected

by the length of $Flan_x$ and the admittance in the y-direction was effected by the length of $Flan_y$.

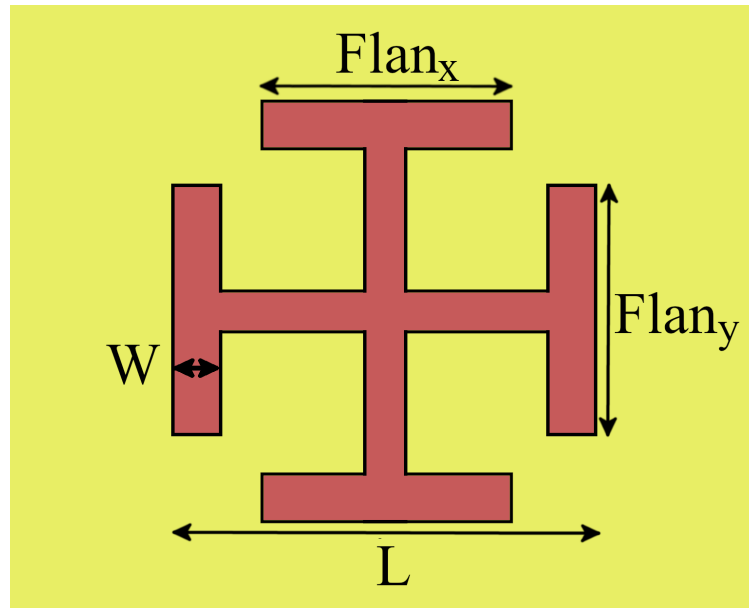


Figure 5.6: Geometry of the chosen unit cell for the layers of the metasurface

After extensive testing, this geometry was chosen for its simplicity of design, as well as its smooth admittance gradient behaviour with respect to the changing side flanges. The admittance profile for this geometry can be seen in Fig. 5.7

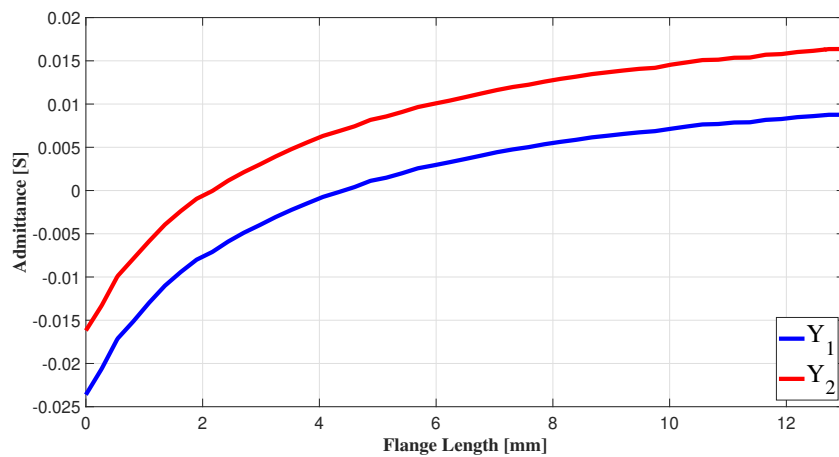


Figure 5.7: Admittance of the unit cell shown in Fig. 5.6 as the flange length is swept

It can be seen that the unit cell shows a very gradual change in the admittance as

the flange length changes, as well as a smooth transition from negative admittance to positive admittance. The gradual change is very useful considering the surface is working under the assumption of local periodicity of unit cells. If the admittance changed very suddenly with respect to the geometric parameter of the unit cell, the assumption of local periodicity between elements would become less valid. This would be due to the possibility of adjacent unit cells with similar admittance values having vastly different physical dimensions. Many unit cells also had very discontinuous values of the admittance when it got close to 0, as well as containing asymptotal behaviour as well, so this geometry is very attractive as it has neither of those behaviours.

Using this database of admittance values per geometric parameter, and the ideal admittance profile of the surfaces, individual unit cells can be matched to the ideal profile. The results of this matching can be seen in Fig. 5.8 and Fig. 5.9 for the TE polarization at 30° steering and in Fig. 5.10 and Fig. 5.11 for the TM polarization at 20° steering.

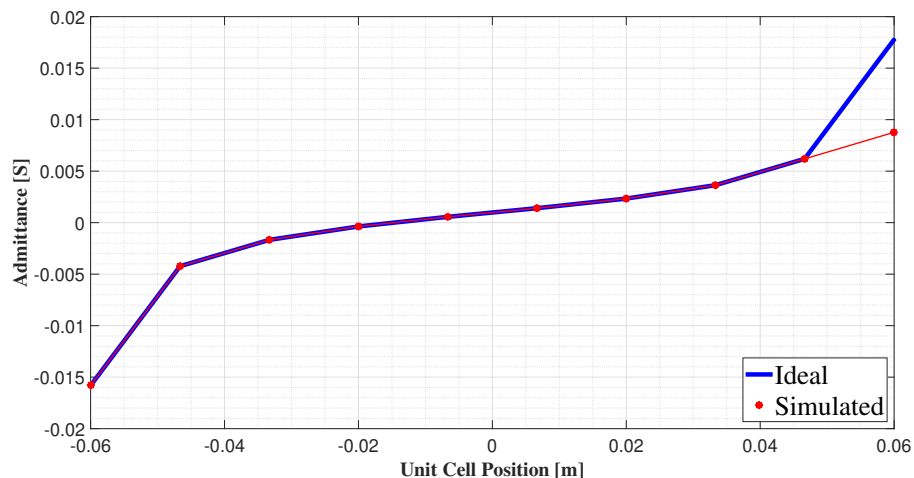


Figure 5.8: Admittance of the unit cell compared to the ideal admittance profile of the outside surface for the TE polarized wave steered at 30°

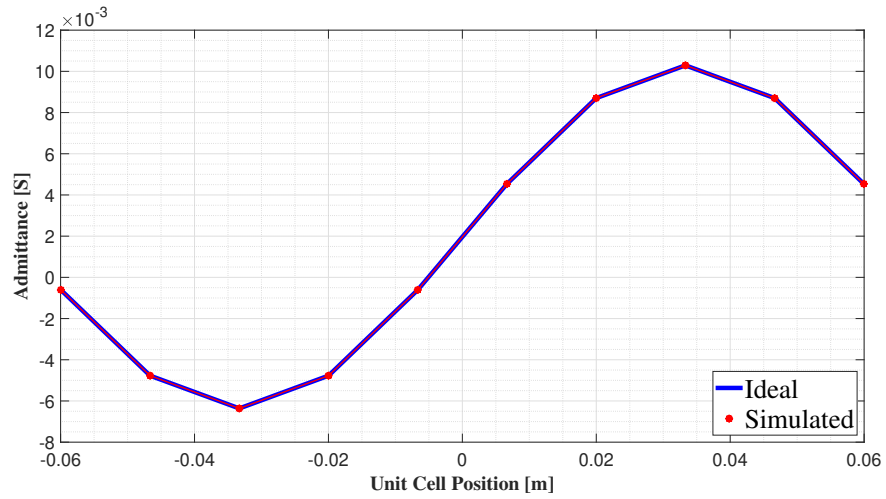


Figure 5.9: Admittance of the unit cell compared to the ideal admittance profile of the inside surface for the TE polarized wave steered at 30°

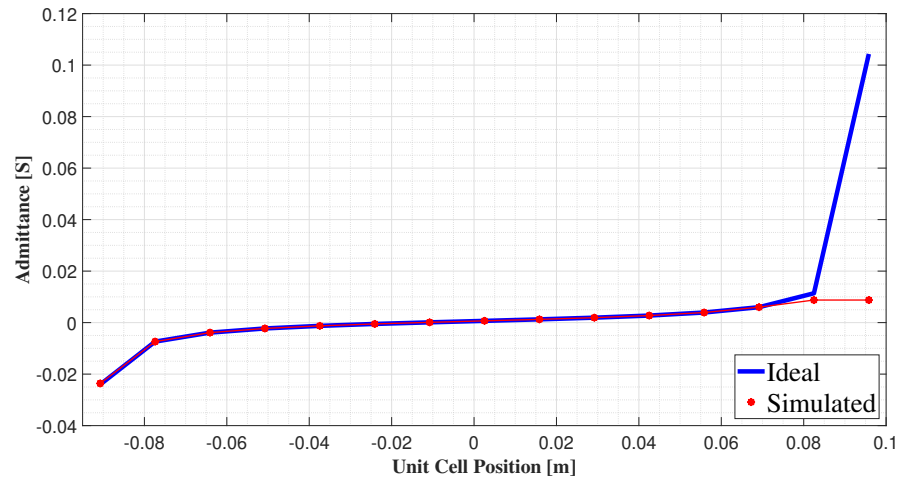


Figure 5.10: Admittance of the unit cell compared to the ideal admittance profile of the outside surface for the TM polarized wave steered at 20°

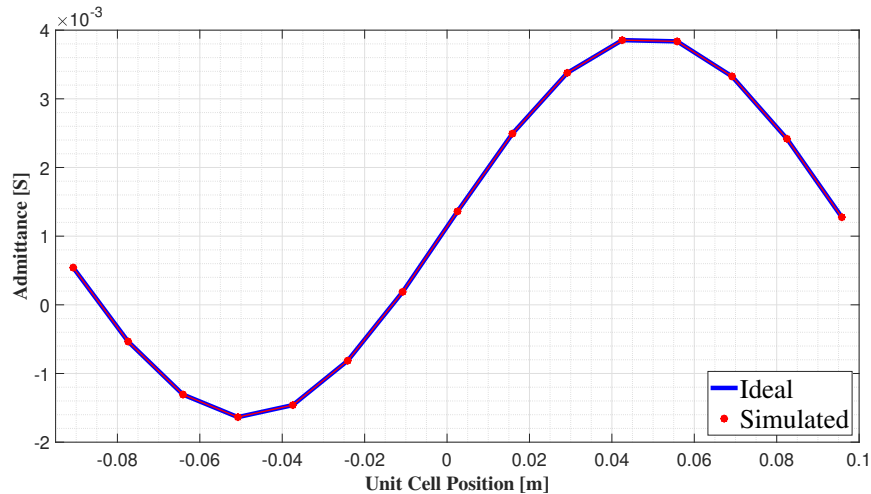


Figure 5.11: Admittance of the unit cell compared to the ideal admittance profile of the inside surface for the TM polarized wave steered at 20°

It can be seen that for most of the surfaces, the admittances match almost perfectly between the ideal and simulated values. There are some discrepancies in the matching for the outside layers, but this is mainly due to the nature of the ideal admittance profiles. The ideal profiles for Y_1 were derived using tangent functions, which naturally have asymptotic points. As such, on either end of the admittance profile there are asymptotes that show the admittance going to positive and negative infinity. This behaviour is masked due to the way that the profile was sampled for the unit cell matching, but become apparent at the edges where the geometry cannot compensate for an infinite admittance. This mismatch is not a large problem for the actual screen, as the problem unit cells are at the edge of the surface. Since the surface is excited at the center of its structure, only a small portion of the field that is low in magnitude interacts with these mismatched unit cells. Due to this, the amount of error from this discrepancy is minimal.

The total surface was constructed in Comsol's Radio Frequency module in order to simulate the response of the structure to an incident wave. For these simulations, a Gaussian beam was used to excite the metasurface in order to see the full field response across a single period of the structure. The surface was as tested with

alternating perfect electric conductor (PEC) and perfect magnetic conductor (PMC) boundaries in order to simulate the structure as inside of a parallel plate waveguide. Simulating the structure in a waveguide was essential in order to align the electric field in each polarization, ensuring that the surface encountered a purely TE or TM incident wave. A parallel plate waveguide achieves this behaviour through by placing the PEC boundaries on the boundaries normal to the direction of the electric field in each polarization, and since electric fields tend to flow from one PEC boundary to another PEC boundary the electric field is distributed evenly in the direction of the electric field. The PMC boundaries achieve the same effect as the PEC boundaries, but affect the magnetic field instead which further supports the polarization of the incoming wave. This constructed structure can be seen in Fig. 5.12.

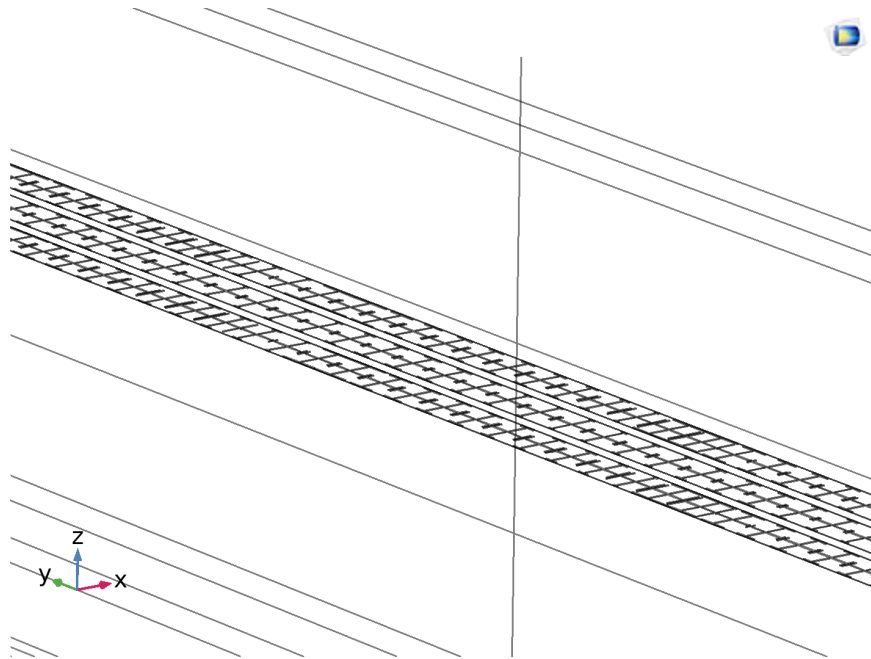


Figure 5.12: Close up on one period of the metasurface constructed in Comsol

This structure was constructed with an additional two periods of the full structure on either side of the original structure so that the full Gaussian beam could interact with the center period of the structure without the side walls of the structure interfering with said Gaussian beam. The repeated structure also allowed for the transmitted

beam to be seen much more easily, as there was more space for the output beam to propagate after transmitting through the screen. The near field distribution given by these simulations can be seen in Fig. 5.13 for the TE polarization steered at 20° and in Fig. 5.14 for the TM polarization steered at 30° .

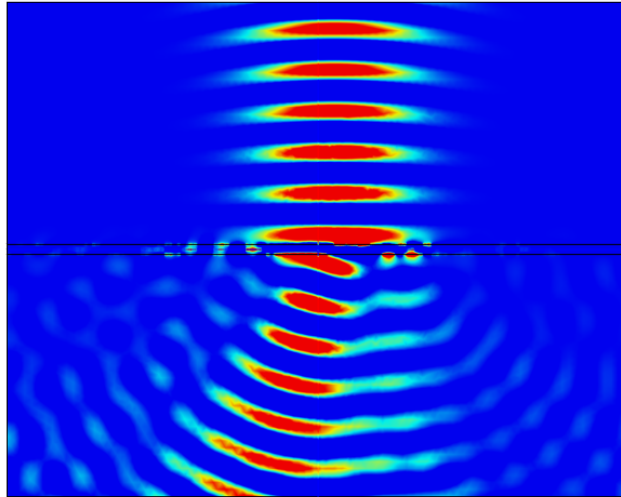


Figure 5.13: Near electric field response for the metasurface designed to steer 20° when excited with a TE Gaussian beam

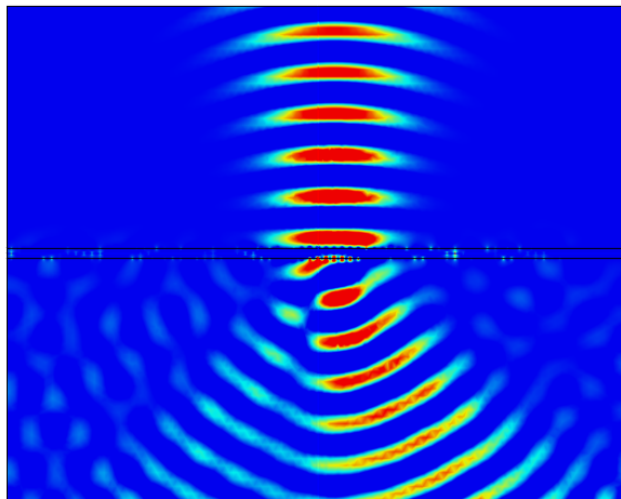


Figure 5.14: Near electric field response for the metasurface designed to steer 30° when excited with a TM Gaussian beam

In these field distributions, there is a clear steering effect happening in both polarization excitations. There is some spreading of the output beam after it passes

through the structure, but since the beam exciting the structure is a Gaussian beam, some spreading after the surface is to be expected. It can also be seen that the distribution shown in Fig. 5.14 shows more spreading than the fields in Fig. 5.13. This is due to the structure being less able to support steering angle of much higher angles than 30° very accurately, and as a consequence there are more errors in the outgoing beam. This behaviour can be gleaned by observing the structural period of the metasurface as the transmitted angle changes. This can be seen in Eq. 5.14, where it becomes apparent that the overall length of the metasurface decreases as the angle increases. This decrease in length, coupled with the fact that the same size unit cells are used for polarization in order to construct a single structure, leads to a decrease in the overall number of unit cells that can populate the surface. In essence, the decreased number of unit cells leads to a decreased number of points that can be used to sample the admittance curves in order to create a continuous admittance profile. This consequence leads to a more stepped profile of the admittance, with larger differences between local unit cells, pushing the concept of local periodicity with respect to admittance to its limits. This behaviour can be seen in Table 5.1, where the angle of refraction, length of one structural period of the surface, and number of unit cells is compared. This table is using the same quantities as the project, that is to say that the surface is designed to operate at $4.5GHz$ and the unit cell size is set to $\frac{\lambda}{6}$.

Table 5.1: Comparison of refraction angle to the total length of the metasurface and the number of unit cells per structural period

Refraction Angle	Length of Surface	Number of Unit Cells
10°	383.92mm	29
20°	194.92mm	15
30°	133.33mm	11
40°	103.72mm	8
50°	87.03mm	7

CHAPTER 6: Conclusions

Overall, there are several distinctions between the two theories which give each approach certain advantages, but which ultimately show that the local transmission line model theory is more applicable in general. The two theories distinguish themselves in their approach to handling the incoming wave. For the local transmission line theory, the incoming wave is treated as a signal traveling through a transmission line circuit. The incoming signal is shaped using transmission line analysis methods to allow for the incoming wave to flow from the input port to the output port with perfect transmission and an altered phase. This designed transmission line circuit is then approximated as a two dimensional sheet in space which interacts with an incoming wave. In essence, the local transmission line model focuses on transforming the incoming wave into an altered version of itself at the output. In contrast to the local transmission line theory, the Huygens-Fresnel theory primarily deals with utilizing the incoming wave as a source to generate a desired output field structure. This generation of a new wave from the incoming wave is made possible by the inclusion of the electric and magnetic dipoles in the unit cells. These dipoles are excited by the incoming wave, and generate waves on either side of the surface. The generated wave at the incoming side of the surface is used to destructively interfere with the remaining portions of the incoming wave, so that no total reflections are noticed. The fields generated by the dipoles on the output side of the surface manifest as the resulting propagating wave, so there is an effective transmission of energy from input to output.

The local transmission line modelled metasurface tends to have a simpler design process, as transmission line circuits are widely used so the analysis methods used in

this design approach are more approachable. The fact that the waves at the input and output of the surface are essentially the same propagating field also assists with calculations and conceptualization. Dividing the surface into three distinct layers also allows for more ease of design, as a three layer approach to metasurfaces allows for enough degrees of freedom in the design for perfect transmission to be viable alongside an inserted phase shift. The three separate layers also allow for the unit cell structure to be more forgiving in their design. By only evaluating each layer separately, the layers can swapped out for another if a unit cell geometry with a different admittance profile is desired. In comparison to the Huygens-Fresnel method, where the unit cells each have to be specifically designed for at each position on the surface, which may necessitate upwards of ten or more unique geometries compared to the three geometries required by the transmission line theory. This fact allows for the local transmission modelled theory to be more versatile than the Huygens-Fresnel theory in its design. In addition, the local transmission line theory can also be theoretically expanded upon into more than two distinct input polarizations. It is theoretically possible to allow for three or more distinct polarizations to have separate steering angles, as long as appropriate unit cell structures are designed.

A disadvantage to using the Local Transmission Line theory would be its variable size with respect to the desired output steering angle. As the steering angle becomes larger, the physical size of the surface's period becomes smaller, with limitations on how many unit cells can be fit into one period. If the steering angle becomes too large, there may not be enough space for the chosen unit cells to fully replicate the desired gradient of admittance in each layer. The transmission line modelled surface also has possibilities for error within its design, if the distance between each admittance layer is too large, then the angle of propagation between layers must be taken into account. For this theory to be valid, the admittance layers are assumed to have normal incidence within the layers, so the distance between layers is kept electrically

small. However, the layers must not be too close to one another as the admittance layers must be electrically separate from one another. Since the unit cell testing was done such that each layer was analyzed distinctly, if the layers were too close then unwanted coupling could occur. This coupling effect could change the admittance of each layer such that the desired steering effect would be greatly reduced or even disappear altogether.

The Huygens-Fresnel theory's focus on re-radiation of the energy delivered by the incoming wave has its own advantages and disadvantages. An advantage of this design technique is in its versatility. Since the structure is creating its own outgoing propagating wave, the resulting wave can be tailored to different applications. These applications include large steering angles, or even generating a wave that has a different polarization from the incoming wave.

Several disadvantages involved in the Huygens-Fresnel theory include the complexities in generating several waves from the surface, as well as speed of design. The Huygens' surfaces must generate a wave at the input of the surface, which is an additional component that is needed to be designed for when compared to the transmission line model. As such, it is generally more difficult to find proper unit cell structures which adhere to these constraints. These unit cell structures are also time consuming to test, as there needs to be a unique geometry for each position on the surface. Each of these geometries must have different transmission phases, and as such, if the surface is for example ten unit cells in length, there needs to be ten unique unit cell geometries across the surface. In comparison to the local transmission line model theory, which only requires one geometry for each of the three layers regardless of the length of the metasurface, the Huygens-Fresnel theory takes a significantly higher amount of time to choose unit cell geometries. Finally, the Huygens-Fresnel theory requires that the dipole structures be normal to the incoming electric field, which eliminates the possibility of creating a multi-polarization type structure as was seen

in the transmission line modelled design.

Taking into account both theories with their advantages and disadvantages, the local transmission line theory is a more versatile and general approach for designing metasurfaces. If an application demands a less complex design, with the possibility of steering multiple beams simultaneously, then the local transmission line modelled theory is more desirable. This theory is also more desirable for use in printed circuit board (PCB) designs, as the admittance sheets can be constructed completely using existing PCB technology on the dielectrics it will be used with. However, more specialized behaviour is not as realizable from the metasurface designed this way. As such, if very large steering angles or arbitrary wave polarization control is desired, then the Huygens-Fresnel theory has more of an advantage. However, the Huygens-Fresnel approach requires a larger amount of time needed to be dedicated as the creation process for the unit cells is much more complex. Since this theory demands separated unit cells, traditional PCB construction is less practical. Since the unit cells must be normal to the incident electric field, creating a metasurface which controls several distinct polarizations is unachievable. As such, this method is recommended for more complex and demanding applications, where exotic behaviour may be needed and more time can be dedicated the design.

As can be seen, the local transmission line design methodology is more practical for most commonplace metasurface applications. The ease of design as well as the more approachable theory make this a more attractive option. The possibility for controlling multiple polarizations in the same structure is also a unique advantage to this specific design theory. In comparison to the Huygens-Fresnel metasurface theory, which has a more complex and time consuming unit cell design process, more opportunities for error in the unit cell designs, as well as the inflexibility for multiple polarizations control, the local transmission line theory is more advantageous in most metasurface applications.

REFERENCES

- [1] L. Zeng and R. Song, “Cloaking of heat flux and temperature,” 2011.
- [2] S. Narayana and Y. Sato, “Heat flux manipulation with engineered thermal materials,” *Phys. Rev. Lett.*, vol. 108, p. 214303, May 2012.
- [3] H. H. Huang and C. T. Sun, “Anomalous wave propagation in a one-dimensional acoustic metamaterial having simultaneously negative mass density and young’s modulus,” *The Journal of the Acoustical Society of America*, vol. 132, no. 4, pp. 2887–2895, 2012.
- [4] J. B. Pendry, A. J. Holden, D. J. Robbins, and W. J. Stewart, “Magnetism from conductors and enhanced nonlinear phenomena,” vol. 47, pp. 2075–2084, 1999.
- [5] R. A. Shelby, D. R. Smith, S. C. Nemat-Nasser, and S. Schultz, “Microwave transmission through a two-dimensional, isotropic, left-handed metamaterial,” vol. 78, pp. 489–491, 2001.
- [6] M. Chen and G. V. Eleftheriades, “Omega-bianisotropic wire-loop huygens’s metasurface for reflectionless wide-angle refraction,” *IEEE Transactions on Antennas and Propagation*, vol. 68, no. 3, pp. 1477–1490, 2020.
- [7] D. M. Pozar, *Microwave Engineering*. John Wiley Sons, Inc., 4 ed., 2012.
- [8] D. S. Parry Moon, *Field theory handbook: Including coordinate systems, differential equations, and their solutions*. Springer-Verlag Berlin Heidelberg, 1988.
- [9] R. Kshetrimayum, “A brief intro to metamaterials,” *IEEE Potentials*, vol. 23, pp. 44–46, 2005.
- [10] M. Kadic, T. B̃eckmann, R. Schittny, and M. Wegener, “Metamaterials beyond electromagnetism,” vol. 76, p. 126501, 2013.
- [11] K. P. Vemuri, F. M. Canbazoglu, and P. R. Bandaru, “Experimental verification of heat flux bending in multilayered thermal metamaterials,” 2014.
- [12] A. Mirabolghasemi, H. Akbarzadeh, D. Rodrigue, and D. Therriault, “Thermal conductivity of advanced architected cellular materials,” 2018.
- [13] F. Chen and D. Y. Lei, “Experimental realization of extreme heat flux concentration with easy-to-make thermal metamaterials,” vol. 5, 2015.
- [14] T. Han, X. Bai, J. T. L. Thong, B. Li, and C.-W. Qiu, “Full control and manipulation of heat signatures: Cloaking, camouflage and thermal metamaterials,” vol. 26, pp. 1731–1734, 2014.
- [15] R. Hu, B. Xie, Q. Chen, J. Cheng, and X. Luo, “Carpet thermal cloak realization with layered thermal metamaterials: Theory and experiment,” 2016.

- [16] L.-M. Hao, C.-L. Ding, and X.-P. Zhao, “Tunable acoustic metamaterial with negative modulus,” vol. 106, pp. 807–811, 2012.
- [17] S. H. Lee, C. M. Park, Y. M. Seo, Z. G. Wang, and C. K. Kim, “Composite acoustic medium with simultaneously negative density and modulus,” *Phys. Rev. Lett.*, vol. 104, p. 054301, Feb 2010.
- [18] H. Chen and C. T. Chan, “Acoustic cloaking in three dimensions using acoustic metamaterials,” vol. 91, p. 183518, 2007.
- [19] V. M. García-Chocano, R. Graciá-Salgado, D. Torrent, F. Cervera, and J. Sánchez-Dehesa, “Quasi-two-dimensional acoustic metamaterial with negative bulk modulus,” *Phys. Rev. B*, vol. 85, p. 184102, May 2012.
- [20] V. G. Veselago, “The electrodynamics of substances with simultaneously negative values of ϵ and μ ,” *Soviet Physics Uspekhi*, vol. 10, pp. 509–514, apr 1968.
- [21] D. R. Smith, W. J. Padilla, D. C. Vier, S. C. Nemat-Nasser, and S. Schultz, “Composite medium with simultaneously negative permeability and permittivity,” *Phys. Rev. Lett.*, vol. 84, pp. 4184–4187, May 2000.
- [22] C. Huygens, *Treatise on Light*. 1690.
- [23] T. Y. A.-J. F. F. A. Henry Crew, Christaan Huygens, *The wave theory of light; memoirs of Huygens, Young and Fresnel*. American Book Company, 1900.
- [24] D. A. B. Miller, “Huygens’s wave propagation principle corrected.,” *Optics Letters*, vol. 16 18, pp. 1370 – 2, 1991.
- [25] S. R. Rengarajan and Y. Rahmat-Samii, “The field equivalence principle: illustration of the establishment of the non-intuitive null fields,” vol. 42, pp. 122–128, 2000.
- [26] G. V. E. Michael Selvanayagam, “Discontinuous electromagnetic fields using orthogonal electric and magnetic currents for wavefront manipulation,” *Opt. Express*, 2013.
- [27] E. Kuester, M. Mohamed, M. Piket-May, and C. Holloway, “Averaged transition conditions for electromagnetic fields at a metafilm,” *IEEE Transactions on Antennas and Propagation*, vol. 51, pp. 2641–2651, 2003.
- [28] A. Epstein and G. V. Eleftheriades, “Arbitrary power-conserving field transformations with passive lossless omega-type bianisotropic metasurfaces,” *IEEE Transactions on Antennas and Propagation*, vol. 64, pp. 3880–3895, 2016.
- [29] S. A. T. Younes Ra’di, “Balanced and optimal bianisotropic particles: maximizing power extracted from electromagnetic fields,” *New Journal of Physics*, vol. 15, May 2013.

- [30] Z. Wang, Y. Zhang, Y. Feng, and Z. N. Chen, "Beam refraction with an isotropic and ultrathin huygens' metasurface," 2015.
- [31] D. A. Frickey, "Conversions between s, z, y, h, abcd, and t parameters which are valid for complex source and load impedances," vol. 42, pp. 205–211, 1994.
- [32] K. Chen, Y. Feng, F. Monticone, J. Zhao, B. Zhu, T. Jiang, L. Zhang, Y. Kim, X. Ding, S. Zhang, A. Al \tilde{A}^1 , and C. – W. Qiu, "Areconfigurable active huygens' metalens," vol. 29, p. 1606422, 2017.
- [33] A. H. Dorrah and G. V. Eleftheriades, "Peripherally excited phased arrays with practical active huygensâ sources and slot elements," 2020.
- [34] S. Jia, X. Wan, D. Bao, Y. Zhao, and T. Cui, "Independent controls of orthogonally polarized transmitted waves using a huygens metasurface," vol. 9, pp. 545–553, 2015.
- [35] L. Zheng and Y. Zhao, "Generalized snell's law and its verification by metasurface," pp. 364–372, 2021.
- [36] C. Pfeiffer and A. Grbic, "Millimeter-wave transmitarrays for wavefront and polarization control," vol. 61, pp. 4407–4417, 2013.
- [37] F. Monticone, N. M. Estakhri, and A. Alù, "Full control of nanoscale optical transmission with a composite metascreen," *Phys. Rev. Lett.*, vol. 110, p. 203903, May 2013.
- [38] M. Albooyeh, Y. Ra'di, M. Q. Adil, and C. R. Simovski, "Revised transmission line model for electromagnetic characterization of metasurfaces," *Phys. Rev. B*, vol. 88, p. 085435, Aug 2013.
- [39] Z. H. Jiang, L. Kang, T. Yue, W. Hong, and D. H. Werner, "Wideband transmit arrays based on anisotropic impedance surfaces for circularly polarized single-feed multibeam generation in the q-band," *IEEE Transactions on Antennas and Propagation*, vol. 68, no. 1, pp. 217–229, 2020.